Contents lists available at ScienceDirect

Applied Catalysis B: Environmental

Effect of the type of ceria dopant on the performance of Ni/CeO$_2$ SOFC anode for ethanol internal reforming

A.A.A. da Silva [a,b], N. Bion [c], F. Epron [c], S. Baraka [c], F.C. Fonseca [d], R.C. Rabelo-Neto [a], L.V. Mattos [e], F.B. Noronha [a,b,*]

[a] National Institute of Technology, Catalysis Division, Av. Venezuela 82, Rio de Janeiro, 20081-312, Brazil
[b] Military Institute of Engineering, Chemical Engineering Department, Praça Gal. Tiburcio 80, Rio de Janeiro, 22290-270, Brazil
[c] Institut de Chimie des Milieux et Matériaux de Poitiers (IC2MP), University of Poitiers, CNRS, 4 rue Michel Brunet, TSA51106, F86073, Poitiers Cedex 9, France
[d] Instituto de Pesquisas Energéticas Nucleares, IPEN-CNEN/SP, Av. Lineu Prestes 2242, São Paulo, 05508-000, Brazil
[e] Fluminense Federal University, Chemical Engineering Department, Rua Passo da Pátria, 156, Niterói, 24210-240, Brazil

ARTICLE INFO

ABSTRACT

This work studied the effect of the type of ceria dopant on the performance of Ni/CeO$_2$ SOFC anode for ethanol conversion reaction. Ni-based catalysts supported on CeO$_2$ doped with different cations (Gd, Y, Pr, Zr, Nb) were prepared by the hydrothermal method. The addition of dopant to ceria led to the formation of the solid solutions during calcination for all samples, except for CeNb sample due to the low solubility limit. In spite of the high oxygen mobility of ceria-based supports, all catalysts deactivated for ethanol decomposition reaction at 1123 K due to carbon deposition. The large Ni^0 and CeO$_2$ crystallites formed during calcination at high temperature reduced the effectiveness of the mechanism of carbon removal because of the low metal-support interfacial area. The lowest formation of carbon on Ni/CeNb catalyst was attributed to the presence of NiNb$_2$O$_6$ phase. The reduction of this phase leads to the formation of Ni particles covered by NbO$_x$ species, which inhibits carbon formation.

© 2017 Elsevier B.V. All rights reserved.

1. Introduction

The ethanol obtained from biomass has been considered as a promising alternative for energy generation, since it does not contribute to CO$_2$ emissions. Furthermore, in countries like Brazil and USA, the ethanol production and distribution infrastructure are well established.

Ethanol can be directly fed into the anode of solid oxide fuel cells (Direct Internal Reforming Solid Oxide Fuel Cells; DIR-SOFC) and reformed to H$_2$ and CO without the use of an external reformer, which reduces the complexity and cost of the fuel cell systems. Moreover, the H$_2$ produced at the anode side through ethanol reforming is consumed by the fuel cell electrochemical reaction, promoting the ethanol conversion and leading to high efficiency [1–3]. Therefore, in order to obtain good DIR-SOFC performance, anodes must have high electronic and ionic conductivity, high catalytic activity and stability in the operating conditions.

Anodes for SOFC systems are usually based on Ni/yttria-stabilized zirconia (YSZ) cermets [4–7]. When Ni/YSZ anodes operate directly with pure (dry) hydrocarbons or ethanol, a significant carbon deposition has been detected [8]. However, there are only few studies on pure bio-ethanol [8–18] or bio-ethanol/water mixture [19–26] fueled SOFC, and stability tests are rarely found.

Therefore, the major challenge of the DIR-SOFC is the development of an anode that is resistant to carbon deposition under SOFC operation conditions [8].

The traditional SOFC anode contains a high Ni content (at least 30 vol.%) in order to obtain high electronic conductivity. The high Ni loading as well as the high temperature required for sintering the ceramic components (electrodes and electrolyte) during the fabrication of SOFC leads to relatively large NiO particle size. Moreover, NiO has a less refractory character and exhibits faster mobility/coarsening than YSZ (and ceria) at high temperature. Such a behavior is more pronounced after reduction, when metallic Ni particles tend to sinter at relatively low temperatures. The relatively large Ni particles favor carbon formation, when hydrocarbons or bio-ethanol are used directly as a fuel in SOFC. The formation of carbon over metallic particles during steam reforming of ethanol reaction is significantly affected by the crystallite size of metal-

* Corresponding author at: National Institute of Technology, Catalysis Division, Av. Venezuela 82, Rio de Janeiro, 20081-312, Brazil.
E-mail address: fabio.bellot@int.gov.br (F.B. Noronha).

lic particles [8,27]. Silva et al. [27] reported that the deactivation rate decreased with decreasing Co particle size. This was due to the lower amount of carbon deposition over the smallest Co particles. They demonstrated that the small metallic particles contained a lower fraction of exposed terraces atoms, which are responsible for the initiation of carbon deposition.

One strategy to avoid carbon deposition is to reduce the Ni content of anodes. Decreasing Ni content increases metal dispersion, which reduces the formation of carbon, improving the performance of SOFC [28,29]. However, the use of conventional technology to prepare anodes with metal content below 30 vol.% did not provide materials with appropriate conductivity to SOFC applications [30]. Therefore, the use of alternative methods to prepare Ni based anodes with high activity, high stability, high conductivity, and low metal content has been proposed [29,30]

Jasinski et al. [30] prepared Ni/Sm-doped ceria cermets (with Ni content below 15 vol.%) by a net-shape procedure. Electrical measurements revealed that the cermet with 7.5 vol.% exhibited a much higher conductivity (10 S/cm) than the cermet prepared by conventional techniques (0.1 S/cm). For the anode with 14 vol.%, the conductivity (200 S/cm) was like that observed for a cermet with 35 vol.% Ni prepared by a conventional technique. The high dispersion and low sintering temperatures of net-shape technique preserved high surface area and nanocrystalline size of Ni particles. Such features promoted a stable framework of well-connected Ni particles, which percolate at volume fractions below the ones expected for classical percolation theory ($\sim$30 vol.%). Therefore, the microstructural properties of the cermets resulted in high electrical conductivity at relatively low volume fraction of Ni (<30 vol.% Ni), as compared to traditional methods. Moreover, the low Ni loading also reduced the volume change during reduction and oxidation of the anode.

The use of hydrothermal method to prepared Ni- based anodes with low metal contents (5 wt.% Ni and 5 wt.% Ru) inhibited the formation of carbon during oxidative steam reforming (OSR) of propane under SOFC operation conditions [29].

In order to suppress carbon formation and improve the electrical conductivity, some authors [10,11,31] have also proposed the use of redox supports in the composition of SOFC anodes, such as ceria based oxide. In this case, authors claim that the high oxygen mobility of ceria supports promotes the mechanism of carbon removal, which in turn should contribute to the stability of the catalysts on ethanol conversion reactions [32]. Furthermore, doping with cations such as Gd^{3+}, Y^{3+}, Pr^{3+} and Zr^{4+} enhances the mobility of oxygen in ceria and then, increases the oxygen storage capacity (OSC) of the support [33].

Nobrega et al. [13] reported a stable operation of a single SOFC containing an Ir/gadolinium-doped ceria (GDC) catalytic layer under pure ethanol for 150 h. Augusto et al. [15] studied the performance of Ni/GDC both as the anode current collector layer and as a catalytic layer in a single SOFC operating directly on pure ethanol. Carbon deposition was not detected in single cells with Ni/GDC catalytic layer after 50 h of continuous operation under direct (dry) ethanol. This result was attributed to the catalytic properties of the Ni/GDC layer and the operation mechanism of gradual internal reforming, in which the oxidation of hydrogen provides the steam for ethanol reforming, thus avoiding carbon deposition.

The addition of dopants to ceria, such as Gd, Zr, Pr, Y, also improves the ionic and electronic conductivity of ceria [34–36]. The use of Nb as a dopant also increases the electronic conductivity of cerium oxide.

However, most of the studies investigated the performance of Gd-doped ceria based catalysts for the ethanol conversion reactions. There is no systematic study about the effect of the type of ceria dopant on the performance of Ni supported catalysts for ethanol conversion reactions.

Therefore, the aim of this study is to investigate the effect of the type of ceria dopant on the catalytic performance of Ni/CeO_2 under operating conditions of a SOFC anode for ethanol internal reforming (1123 K). The hydrothermal method was used to prepare the Ni/dopant-CeO_2 (dopant = Gd, Zr, Pr, Y, Nb) SOFC anodes with 18 wt.% Ni. The oxygen mobility and the reducibility of the samples were obtained by temperature-programmed reduction (TPR) and isotopic exchange of $^{18}O_2$ with $^{16}O_2$. In situ X-ray diffraction analyses (XRD) were performed to follow the changes on catalyst structure during the reduction and ethanol decomposition (ED) reaction, which might shed light on the mechanism of catalyst deactivation. In addition, the amount and the nature of carbon formed during ethanol decomposition was determined by thermogravimetric analysis (TG) and scanning electron microscopy (SEM).

2. Experimental

2.1. Catalyst preparation

Doped-ceria support was obtained by a hydrothermal method previously described [15]. An aqueous solution containing cerium (IV) ammonium nitrate and the dopant precursor salts (nitrate of gadolinium, yttrium, praseodymium and zirconium; ammonium niobium oxalate) was prepared with a Ce/dopant molar ratio of 9/1. Then, cerium and the dopant hydroxides were co-precipitated through the addition of an excess of ammonium hydroxide. The precipitate was transferred to an autoclave and it was heated to 453 K for 4 h. Then, the precipitate was washed with distilled water and calcined at 573 K for 2 h in a muffle furnace. Ni was added to doped-ceria support by wet impregnation using an aqueous solution of $Ni(NO_3)_2 \cdot 6H_2O$ to obtain 18 wt.% of Ni. After impregnation, the sample was dried at 393 K and calcined under air (50 mL/min) at 1073 K according to the following temperature program: (i) from room temperature to 673 K at 0.5 K/min; (ii) from 673 to 1073 K at 2 K/min and (iii) remained at final temperature for 5 h. The following samples were synthesized: Ni/CeO_2; Ni/CeGd; Ni/CeY; Ni/CePr; Ni/CeZr; Ni/CeNb.

A $NiNb_2O_6/CeO_2$ sample was prepared according to the procedure previously described in the literature [37], by conventional wet impregnation of the CeO_2 support (prepared as mentioned above) with an aqueous solution containing $Ni(NO_3) \cdot 6H_2O$ and ammonium niobium oxalate (CBMM) in a rotary evaporator. The solution was heated at 343 K under continuous stirring for 1 h. Then, the solvent was removed by evaporation under reduced pressure at 363 K, and the resulting solid was dried overnight at 393 K and calcined in synthetic air at 1073 K and 1273 K for 5 h.

2.2. BET surface area

The BET surface area of the samples was measured using a Micromeritics ASAP 2020 analyzer by nitrogen adsorption at the boiling temperature of liquid nitrogen.

2.3. $^{18}O_2/^{16}O_2$ isotopic exchange

Oxygen Isotopic Exchange (OIE) reaction experiments were carried out in a closed recycling system connected to a Pfeiffer Vacuum quadrupole mass spectrometer and a vacuum pump, as described elsewhere [38]. The samples (c.a. 20 mg) were placed into a quartz U-form reactor and pre-treated prior to the experiment: the samples were oxidized under pure $^{16}O_2$ flow (20 mL/min, 973 K, 1 h) and evacuated for 1 h. A treatment under pure H_2 at 973 K was carried out to study the behavior of the reduced samples. After the pre-treatment, samples were cooled down to the reaction temperature.
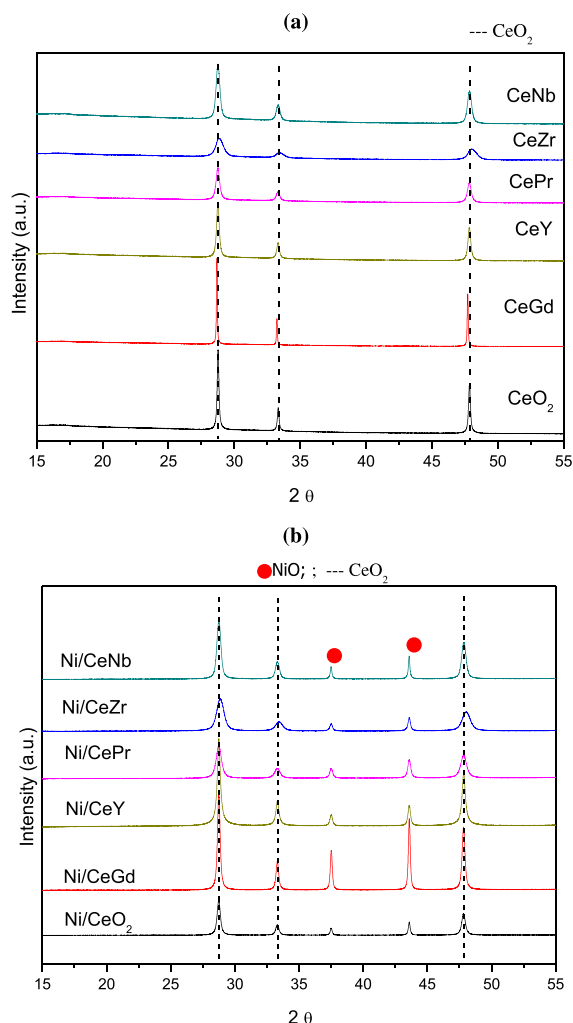
(a)

(b)

Fig. 1. X-ray diffraction patterns obtained for (a) calcined supports (b) calcined samples. (—) CeO_2; (●) NiO.

For the Isothermal Oxygen Isotopic Exchange (IOIE) experiments, the temperatures of reaction were 780 and 878 K. A pressure of 55 mbar of pure $^{18}O_2$ ($\geq$99 at.%, ISOTEC) was introduced and stayed nearly constant during the whole experiment. The evolution of each isotopomer concentration was analyzed by monitoring the following m/z signals: 32 ($^{16}O_2$), 34 ($^{18}O^{16}O$), 36 ($^{18}O_2$). The signals corresponding to m/z = 44, 46, 48, 28 were also recorded to verify the absence of carbon dioxide and air in the system.

For the Temperature-Programmed Oxygen Isotopic Exchange (TPOIE) experiments, pure $^{18}O_2$ was injected at 473 K and the sample was heated at 2 K/min up to 973 K.

The calculations of the exchange rate, R_e (for isothermal experiment), and the number of oxygen exchange (N_e) were calculated from the variation in partial pressures as described in a previous work [39].

2.4. In situ X-ray diffraction (XRD)

In situ XRD was carried out at the XPD–10 B beamline of the Brazilian Synchrotron Light Laboratory (LNLS). The samples were first crushed and homogeneously distributed over the support. The samples were heated in a furnace installed into a Huber goniometer operating in Bragg–Brentano geometry (θ – 2θ). The XRD patterns were obtained by a Mythen – 1 K detector (Dectris) located 1 m from the furnace, in two different conditions: a) 2θ interval from

20° to 85°, b) 2θ interval from 20° to 55°, with a step size of 0.003° and a counting time of 1 s. The wavelength used was 1.55002 Å. Measurements were made while the sample underwent the following treatments: (i) Reduction under a 5% H_2/He mixture from 298 to 1123 K at a heating of 10 K/min, remaining at this temperature for 1 h. After reduction, the sample was purged with helium at the same temperature for 30 min (ii) Ethanol decomposition (ED) under reaction mixture containing 98% He, 2% ethanol at 1123 K for 1 h. The average crystallite size of CeO_2, NiO and metallic Ni under different treatments was calculated using the Scherrer equation.

2.5. Temperature programmed reduction (TPR)

Prior to the TPR experiment, the sample was pre-treated at 673 K for 1 h under a flow of synthetic air to remove traces of water. The reducing mixture (1.5% hydrogen in argon) was flowed through the sample (300 mg) at a flow rate of 30 mL/min and the temperature was increased to 1273 K at a heating rate of 10 K/min.

2.6. Thermogravimetric analysis (TG)

Temperature programmed oxidation (TPO) experiments were performed using a Shimadzu (TG – 60) equipment to determine the amount of carbon formed over the used catalyst. The analysis was carried out after ED reaction at 1123 K. Approximately 10 mg of spent catalyst was heated under air flow from room temperature to 1273 K at a heating rate of 20 K/min and the weight change was measured.

2.7. Scanning electron microscopy (SEM)

SEM analyses of the spent catalysts were carried out using a FEI Inspect S scanning electron microscope equipped with a secondary electron analyzer. The microscope was also equipped with an EDAX analytic system energy dispersive spectrometer (EDS). The samples were reduced following the same conditions previously described in XRD section.

2.8. Transmission electron microscopy (TEM)

Transmission electron microscopy (TEM) analyses were performed for both as-prepared and reduced Ni/CeGd and Ni/CeNb catalysts. Images were acquired using a 200 kV JEOL microscope, model JEM-2100. Energy dispersive X-ray analysis was performed for local chemical analysis (in TEM mode). For some samples, mapping was performed in High Angle Annular Dark Field (HAAF) Scanning Transmission Electron Microscopy (STEM) mode. Samples were prepared by dispersing the powder with isopropanol onto the surface of the Cu sample holder for TEM analyses.

2.9. Reaction conditions

Ethanol decomposition (ED) reaction was performed using a fixed-bed reactor at atmospheric pressure for all catalysts studied. Prior to reaction, samples were reduced under pure hydrogen (30 mL/min) at 1023 K for 1 h and then purged under N_2 at the same temperature for 30 min. All reactions were carried out at 1123 K, which is the typical reaction temperature for the internal reforming over SOFC anodes. For ED, N_2 (30 mL/min) was passed through the saturator containing ethanol, and then the reactant mixture obtained was diluted with N_2 (each N_2 stream flowed at 30 mL/min). The partial pressure of ethanol was maintained constant for all experiments. In order to observe the catalyst deactivation within a short timeframe, a small amount of catalyst was used (20 mg). The samples were diluted with SiC (SiC mass/catalyst mass = 3.0). The reaction products were analyzed by
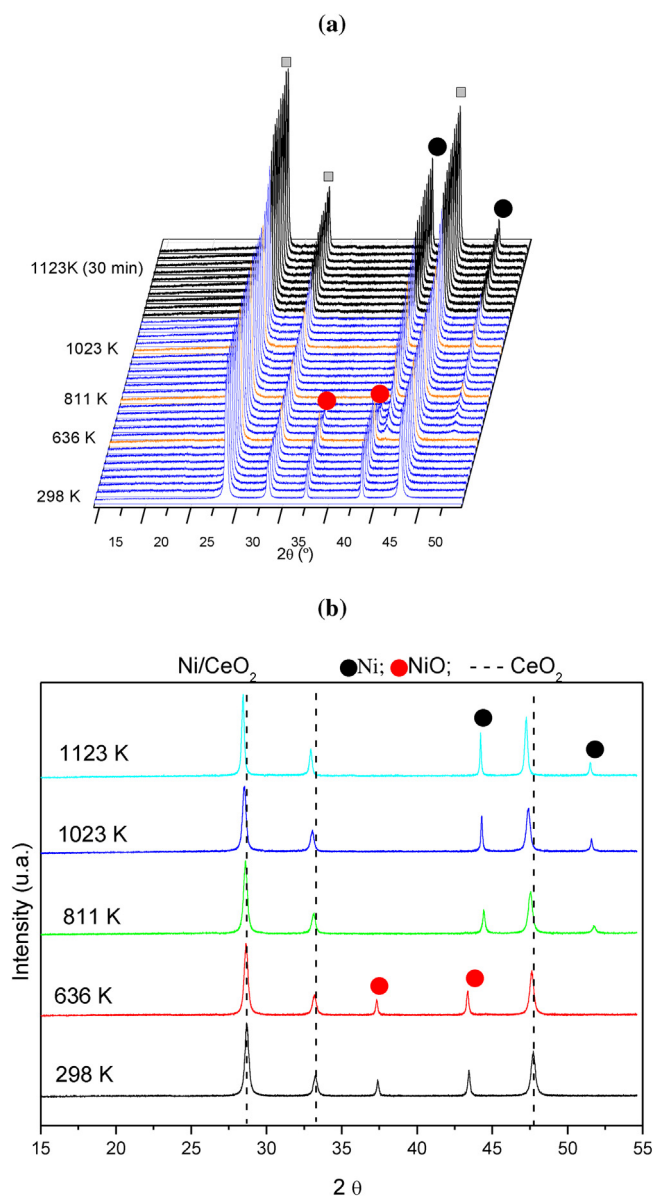
(a)

(b)

Fig. 2. X-ray diffraction patterns obtained for Ni/CeO$_2$ (a) during reduction from room temperature to 1123 K; (b) selected temperatures (orange curves). (■) CeO$_2$; (● red) NiO; (● black) Ni. (For interpretation of the references to colour in this figure legend, the reader is referred to the web version of this article.)

gas chromatography (Micro GC Agilent 3000 A) containing three channels with three thermal conductivity detectors (TCD) and three columns: a molecular sieve, a Poraplot Q and OV-1 column. The ethanol conversion (X$_{ethanol}$) and product distribution (S$_x$) were determined as follows:

$$X_{ethanol} = \frac{(n_{ethanol})_{fed} - (n_{ethanol})_{exit}}{(n_{ethanol})_{fed}} \times 100 \qquad (1)$$

$$S_x = \frac{(n_x)_{produced}}{(n_{total})_{produced}} \times 100 \qquad (2)$$

where (n$_x$)$_{produced}$ = moles of x produced (x = hydrogen, CO, CO$_2$, methane, acetaldehyde or ethylene) and (n$_{total}$)$_{produced}$ = moles of H$_2$ + moles of CO + moles of CO$_2$ + moles of methane + moles of acetaldehyde + moles of ethylene (i.e., the moles of water produced are not included).

Table 1
BET surface area of supports and catalysts.

Sample	Surface Area (m^2/g)
Ni/CeO$_2$	15 (<10)[a]
Ni/CeGd	15 (12)
Ni/CeY	14 (<10)
Ni/CePr	11 (18)
Ni/CeZr	24 (39)
Ni/CeNb	16 (23)

[a] The values in the parenthesis corresponds to the BET surface area of the supports.

Table 2
Lattice parameter of CeO$_2$ for all catalysts under different conditions.

Sample	Lattice parameter (A)		
	Calcined	Reduced 1023 K	Reduced 1123 K
Ni/CeO$_2$	5.4054 (5.4033)[a]	5.4485	5.4654
Ni/CeGd	5.4074 (5.4192)[a]	5.4495	5.4595
Ni/CeY	5.4068 (5.4056)[a]	5.4504	5.4654
Ni/CePr	5.4072 (5.4064)[a]	5.4997	5.5112
Ni/CeZr	5.3870 (5.3827)[a]	5.4527	5.4720
Ni/CeNb	5.4064 (5.4051)[a]	5.4545	5.4748

[a] The values in the parenthesis corresponds to the lattice parameter of the supports.

3. Results and discussion

3.1. Catalyst characterization

Table 1 shows the BET surface area obtained for all supports and catalysts. The BET surface area was low for all materials due to the relatively high calcination temperature required for SOFC processing. Augusto et al. [15] also obtained a low BET area (8 m^2/g) for a Ni/CeGd sample prepared by the method used in this work.

Adding Nb, Zr or Pr to CeO$_2$ increased the surface area of the supports Such an increase was more significant for the sample doped with Zr. Several authors [40–42] obtained similar results for Zr-doped CeO$_2$. The presence of Zr increases the thermal stability of CeO$_2$, inhibiting particle coarsening [33,40]. The same results were reported in the literature for the addition of Nb and Pr to CeO$_2$ prepared by the precipitation method [43–45]. On the other hand, no significant change in surface area was observed for CeO$_2$ doped with Gd or Y. The impregnation of NiO increased the specific surface area with respect to the ones measured for ceria supports for Ni/CeO$_2$, Ni/CeGd and Ni/CeY. On the other hand, the surface area of NiO/doped-ceria samples decreased for the remaining dopants (Pr, Zr, and Nb). All catalysts exhibited comparable surface area (~15 m^2/g), except for Ni/CeZr, which maintained a higher value (~24 m^2/g) after the impregnation of NiO.

Fig. 1a shows the XRD patterns of different ceria-based calcined supports (CeO$_2$, CeGd, CeY, CePr, CeNb and CeZr). The diffractograms of all samples exhibited the lines corresponding to CeO$_2$ with cubic structure (ICSD 34-394). However, as compared to the pattern of CeO$_2$, shifts of the diffraction lines to lower 2θ positions were observed for CeGd, CeY, CePr, and CeNb, while for CeZr sample the diffraction lines were shifted to higher 2θ values. The lattice constant (a) of CeO$_2$ was calculated from the (111) reflections and listed in Table 2. The calculated value for CeO$_2$ is close to the nominal one [46] and the observed variation upon doping with different cations is consistent with the ionic radius of the dopant. Doping ceria with Gd^{3+}, Y^{3+}, and Pr$^{3+/4+}$ increased the lattice constant, whereas the addition of Zr^{4+} decreased the lattice parameter. The results obtained agree with data reported in the literature [46–48]. Thus, the calculated lattice constants suggest the formation of solid solutions during calcination of the samples: Ce$_{0.9}$Gd$_{0.1}$O$_{1.95}$ (JCPDS 75-0161), Ce$_{0.9}$Y$_{0.1}$O$_{1.95}$ (JCPDS 01-075-0174), Ce$_{0.9}$Pr$_{0.1}$O$_{1.95}$ (ICSD

Table 3

Crystallite size of CeO_2 calculated through X-ray diffraction patterns obtained for calcined samples, during reduction under H_2 at different temperatures and under reaction conditions.

Samples	$dCeO_2$ (nm)			
	Calcined	Reduced 1023 K	Reduced 1123 K	Reaction 1123 K
Ni/CeO$_2$	25	26	53	53
Ni/CeGd	30	33	61	69
Ni/CeY	25	25	31	29
Ni/CePr	15	20	47	54
Ni/CeZr	10	11	14	16
Ni/CeNb	21	21	23	22

Table 4

Crystallite size of NiO and Ni^0 calculated through X-ray diffraction patterns obtained for calcined samples, during reduction under H_2 at different temperatures and under reaction conditions.

Samples	d_{NiO} (nm)	d_{Ni} (nm)			
	Calcined	Reduced 813 K	Reduced 1023 K	Reduced 1123 K	Reaction 1123 K
Ni/CeO$_2$	50	25	67	99	84
Ni/CeGd	47	45	91	133	143
Ni/CeY	33	27	48	71	80
Ni/CePr	29	21	39	63	74
Ni/CeZr	28	23	33	43	46
Ni/CeNb	56	57	100	124	124

182184) and $Ce_{0.9}Zr_{0.1}O_{1.95}$ (ICSD 152478). A notable exception is CeNb. Nb^{4+} (coordination number 8) has a much smaller ionic radius (0.79 Å) as compared to the other dopants and the host cation Ce^{4+} (ionic radius 0.97 Å) that is likely to result in large lattice distortions and, thus, a lower solid solution range. Indeed, as the niobium content used (5.2 wt.%) is higher than the solubility limit of Nb in CeO_2 (1.4 wt.%) [49], secondary phases such as Nb_2O_5, and $CeNbO_{4.26}$ might be formed. However, niobia-rich secondary phases were not detected in the XRD analyses, which is probably because they have high dispersion and low relative volume fraction.

Fig. 1b shows the XRD patterns of the Ni/CeO$_2$, Ni/CeGd, Ni/CeY, Ni/CePr Ni/CeZr and Ni/CeNb calcined samples. The diffractograms of all catalysts exhibited the lines corresponding to the cubic structure of CeO_2 (ICSD 34-394) and NiO (JCPDS 24018). However, only a slight shift of the CeO_2 diffraction lines was observed for Ni/CeGd, Ni/CeY, Ni/CePr, Ni/CeZr and Ni/CeNb due to the formation of the solid solution. For the catalysts, the lattice parameters presented in Table 2 show the same trend observed for the supports. However, the variation in the lattice parameter of CeO_2 caused by the addition of dopant was less significant for the NiO/doped-ceria in comparison to the support. This might be due to the migration of Ni^{2+} into the ceria lattice and the formation of $Ce_{1-x}Ni_xO_{2-y}$ mixed-oxides during calcination [50]. XPS analysis of Ni deposited on a clean CeO_2 (111) surface detected the formation of a $Ce_{1-x}Ni_xO_{2-y}$ mixed metal oxide upon annealing at high temperatures [51]. However, the limit of solubility of Ni in the structure of ceria is low (10–12%) [52]. The insertion of Ni into ceria lattice induces a contraction in the lattice parameter [52], which compensates the variation in the opposite direction caused by the addition of the dopant, resulting in a smaller change in the lattice parameter of the catalysts.

Tables 3 and 4 list the crystallite sizes of CeO_2 and NiO calculated using the Scherrer equation and the CeO_2 (111) and NiO (200) diffraction lines, respectively, for calcined samples. The addition of Pr and Zr led to a decrease in the CeO_2 crystallite size, similarly to previous data for CeO_2-ZrO_2 systems [40–42]. The reduction in the CeO_2 crystallite size is attributed to an increase in the crystallographic disorder in the compounds due to the incorporation of the dopant in the CeO_2 structure [53,54]. The crystallite size depen-

dence on the dopant (Table 3) are in perfect agreement with the BET surface area data (Table 1) and probably reflect variations of the average particle size of the supports.

Calculated crystallite sizes for NiO (Table 4) are larger than that of ceria supports (Table 3). The smallest crystallite sizes of NiO was observed for Ni/CeZr sample. This result is likely due to the higher ceria surface area (CeZr), which led to the formation of more dispersed NiO particles during the calcination step. In the case of the Ni/CeNb, the addition of niobium to ceria did not decrease the NiO crystallite size. Heracleous et al. [54] studied the effect of Nb/Ni molar ratio in the NiO crystallite size obtained for Ni–Nb–O mixed-oxide catalysts. It was observed that the addition of Nb led to a contraction of the NiO lattice and a reduction of NiO crystallite size up to a Ni/Nb ratio of 0.176. In our work, the lattice parameter of NiO for the sample Ni/CeO$_2$ was 4.1750 Å, while for the sample Ni/CeNb the value was 4.1747 Å, which indicates that niobium was not incorporated into the nickel oxide lattice.

In situ X-ray diffraction patterns obtained during reduction for Ni/CeO$_2$, Ni/CeGd and Ni/CeNb samples are shown in Figs. 2 a, 3 a and 4 a . The changes in the diffractograms during reduction can be followed in more detail in Figs. 2 b, 3 b and 4 b. The diffractograms of other ceria-doped samples are presented in the supplementary information (Figs. S1–S3 in the online version at DOI: http://dx.doi.org/10.1016/j.apcatb.2017.01.069). For Ni/CeO$_2$, when the sample was heated from room temperature to 636 K, the CeO_2 diffraction lines shifted to lower 2θ positions. This result is related to the lattice expansion with increasing temperature as it has been reported in the literature [55,56]. However, the lines corresponding to NiO were still observed up to 636 K. Further increase in the temperature to 811 K led to the progressive disappearance of the lines of NiO phase, along with the appearance of the characteristic lines of Ni^0. This result indicates that NiO was completely reduced to Ni^0 at 811 K. It is also noticed that the CeO_2 lines significantly shifted to lower 2θ positions as temperature increased up to 1123 K. This result could be attributed to the partial reduction of CeO_2 to CeO_x promoted by the metallic Ni particles produced and the formation of Ce^{3+} and oxygen vacancies. Since the ionic radius of Ce^{3+} (1.14 Å) is higher than that of Ce^{4+} (0.97 Å), the shift observed in the lines of ceria can be related to this variation in ionic radius and the thermal expansion. In addition, the shift in the ceria lines could also be due to the reduction of the $Ce_{1-x}Ni_xO_{2-y}$ mixed-oxides. According to Barrio et al. [52], the reduction of $Ce_{1-x}Ni_xO_{2-y}$ mixed-oxides involves the reduction of Ce^{4+} species to Ce^{3+} as well as Ni^0 formation. The creation of oxygen vacancies and Ce^{3+} species results in an expansion of the lattice. Xu et al. [56] also observed a non-thermal expansion of the ceria lattice when NiO was reduced during the in situ XRD of a Ni/CeO$_2$ catalyst. This lattice expansion was attributed to the partial reduction of Ce^{3+} to Ce^{4+} with removal of oxygen atoms from the ceria lattice.

In the case of the ceria-doped samples, the diffractograms obtained during reduction exhibited similar behavior. However, comparing the XRD patterns of the ceria-doped samples with those obtained for Ni/CeO$_2$, it was observed that the shift of the ceria lines to lower 2θ positions was more pronounced for the samples containing the dopants Zr, Pr and Nb. This shift increased in the following order: Ni/CeGd < Ni/CeY < Ni/CeO$_2$ < Ni/CeNb < Ni/CeZr < Ni/CePr. These results indicate that the addition of Nb, Zr and Pr improved the reducibility of CeO_2, a feature more pronounced for Ni/CePr. Mogensen et al. [57] compared the expansion of the lattice parameter of both ceria and Gd-doped ceria during reduction at 1273 K. It was noticed that Gd-doped ceria exhibited lower expansion of the lattice parameter than ceria, in good agreement with the present results. The calculated lattice parameters of samples after the reduction at 1023 K and 1123 K are reported in Table 2. For all samples, the lattice parameter expanded during reduction due to
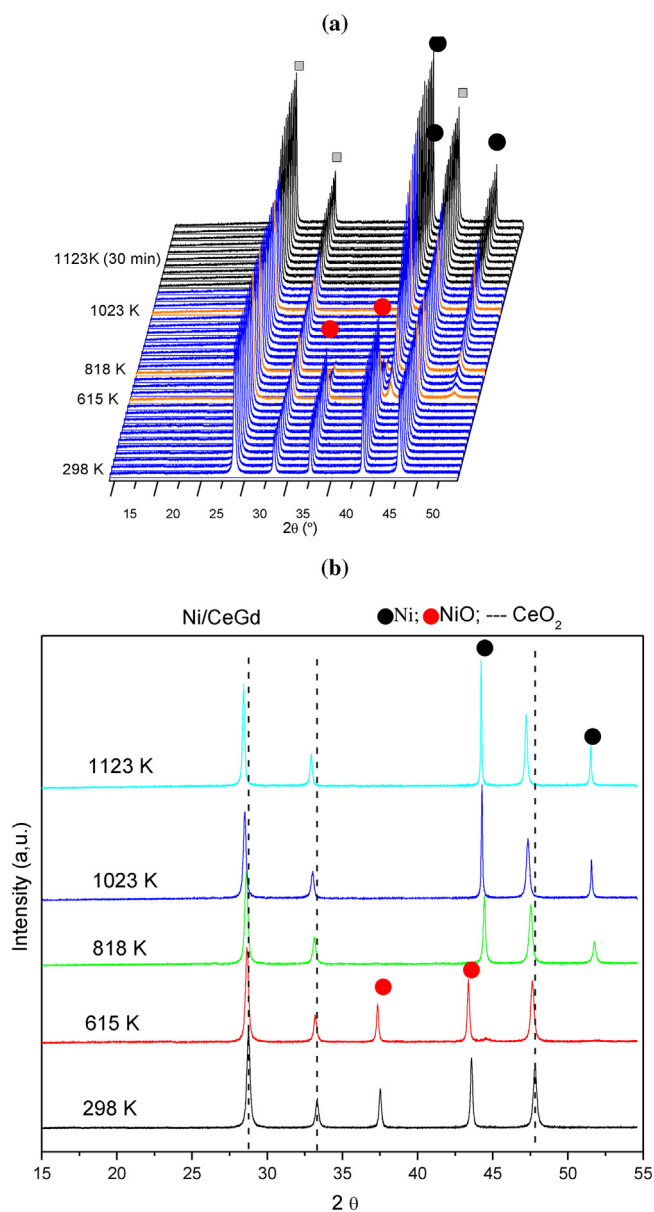
Fig. 3. X-ray diffraction patterns obtained for Ni/CeGd (a) during reduction from room temperature to 1123 (orange curves) K; (b) (orange curves) selected temperatures (orange curves). (■) CeO_2;(●) NiO; (●) Ni.. (For interpretation of the references to colour in this figure legend, the reader is referred to the web version of this article.)
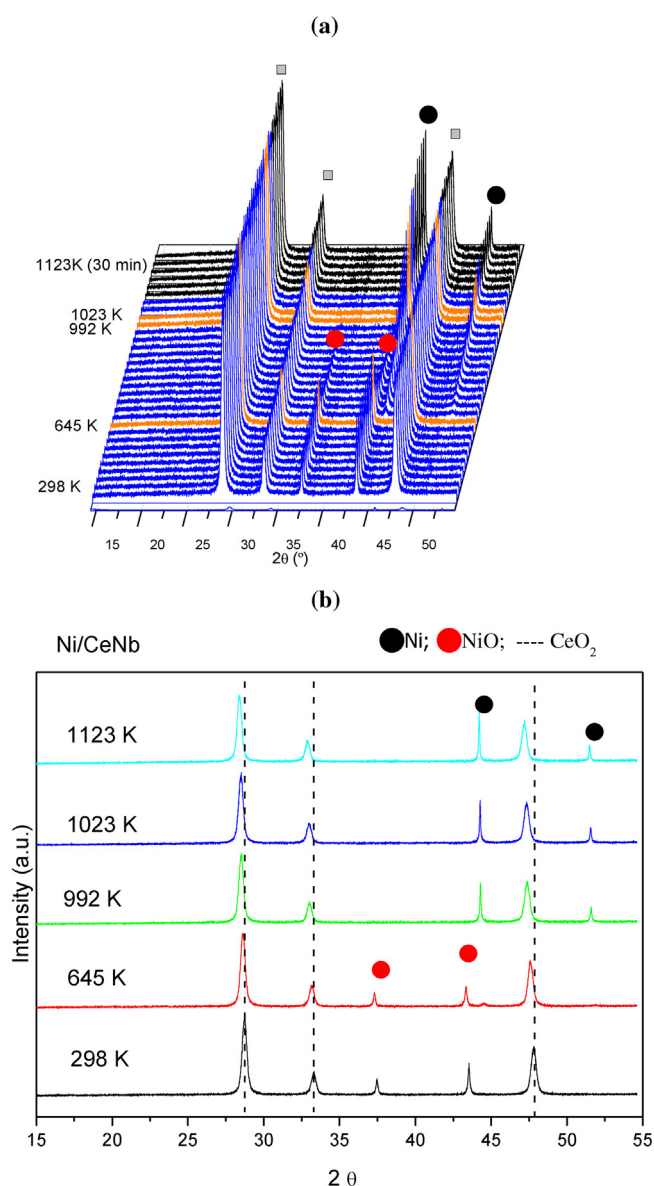

Fig. 4. X-ray diffraction patterns obtained for Ni/CeNb (a) during reduction from room temperature to 1123 K; (b) selected temperatures (orange curves). (■) CeO_2;(●) NiO; (●) Ni. (For interpretation of the references to colour in this figure legend, the reader is referred to the web version of this article.)

the formation of Ce^{+3}, but such expansion is less pronounced for the Gd and Y doped ceria, in good agreement with the literature. The concentration of Ce^{+3} formed during reduction (extent of reduction) was calculated taking in account the lattice parameter measured after reduction at 1273 K and using the procedure proposed by Bonk et al. [46]. The results obtained followed the order: Ni/CeGd (6.54%) < Ni/CeY (6.8%) ≈ Ni/CeO₂ (6.8%) < Ni/CeZr (7.1%) < Ni/CeNb (7.2%) < Ni/CePr (8.8%).

The temperature corresponding to the complete reduction of NiO to Ni⁰ varied depending on the type of the dopant: Ni/CeO₂ (811 K), Ni/CeGd (818 K), Ni/CeY (772 K), Ni/CePr (723 K), Ni/CeZr (823 K) and Ni/CeNb (993 K). The addition of Y and Pr improved the reducibility of NiO whereas the reduction temperature of NiO to Ni⁰ was higher for Ni/CeNb, indicating that the presence of Nb decreased the NiO reducibility. This result suggests that the formation of a Ni–Nb solid solution may be ruled out, since the insertion

of Nb into the NiO structure would weaken the Ni—O—Ni bonds, leading to NiO reduction at lower temperatures [54]. However, the partial coverage of the surface of NiO particles by partially reduced niobium oxides could hinder NiO reduction, increasing the reduction temperature [53].

The average crystallite sizes of CeO_2 and Ni^0 obtained during reduction under H_2 at different temperatures are shown in Tables 3 and 4. Increasing the reduction temperature to 1023 K slightly increased the CeO_2 crystallite size for all samples (Table 3). However, further increase in the temperature to 1123 K produced a significant growth of the CeO_2 crystallite size for Ni/CeO₂, Ni/CeY, Ni/CePr and, more markedly, Gd-doped catalyst. However, no significant changes in CeO_2 crystallite size were detected for the sample containing Nb.

The increase in the reduction temperature significantly increased the Ni^0 crystallite size for all catalysts (Table 4). After reduction at 1123 K, large metallic Ni crystallites (43–133 nm) were obtained for all samples. The largest metallic Ni crystallite size was
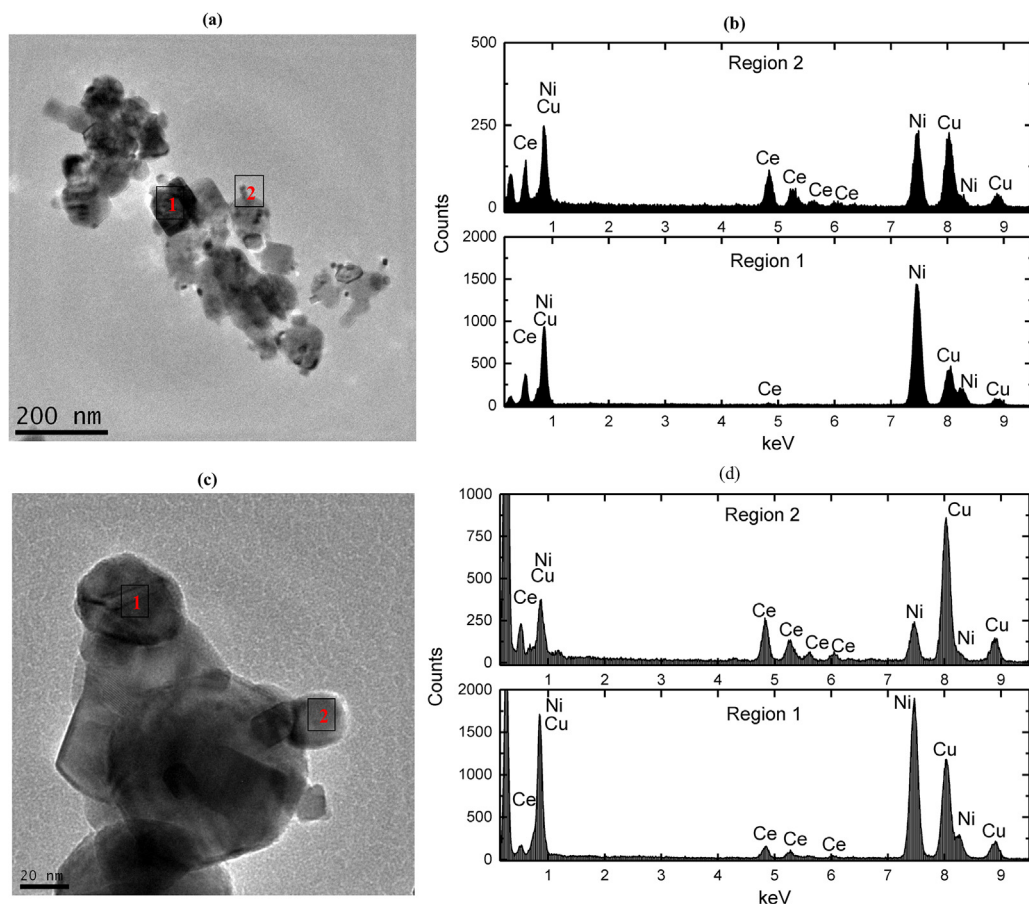
Fig. 5. (a) TEM image of NiO/CeGd (calcined); (b) EDX of selected particles: (c) TEM image of Ni/CeGd (reduced); (d) EDX of selected particles.
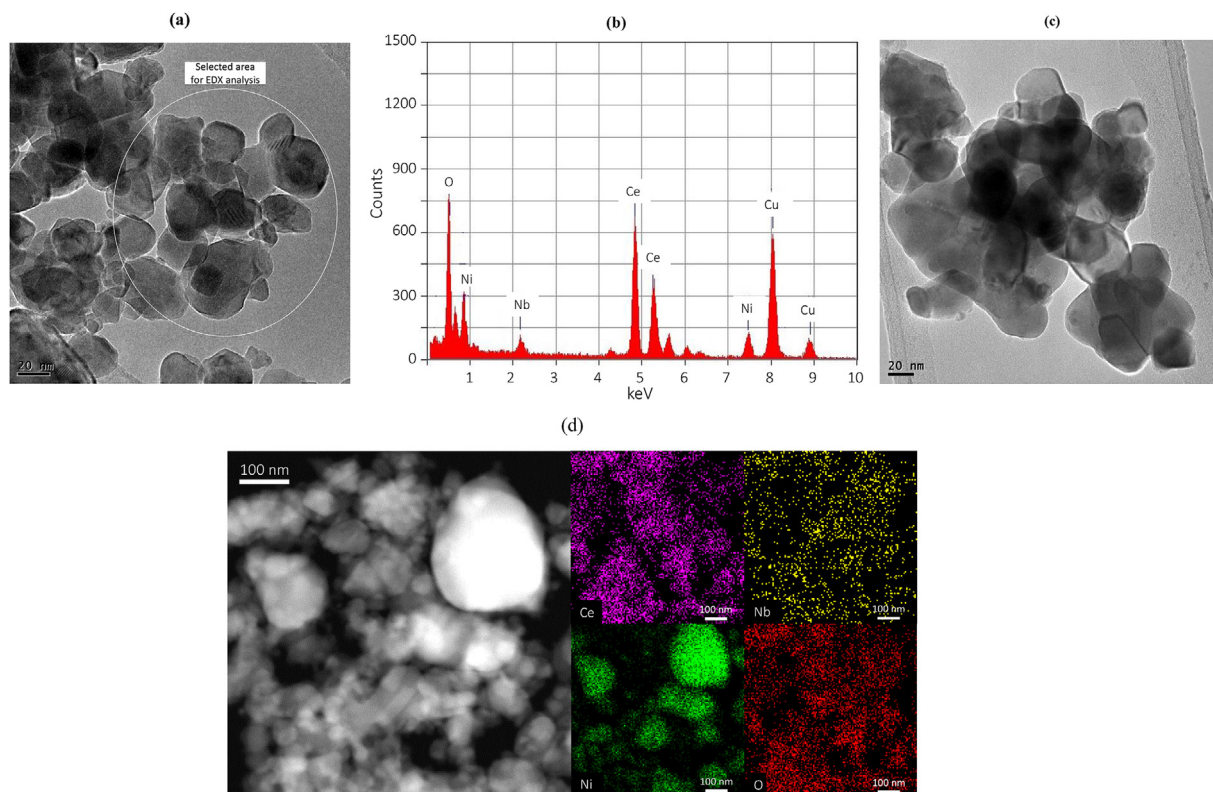

Fig. 6. (a) TEM image of NiO/CeNb (calcined); (b) EDX of selected area: (c) TEM image of Ni/CeNb (reduced); (d) STEM image of reduced catalyst with corresponding chemical mapping.

Table 5
Amount of H_2 consumed and reduction degree of the supports and NiO obtained during TPR analyses.

Sample	Low temperature region (600–900 K) $\mu.mol/g_{cat}$	High temperature region (900–1273 K) $\mu.mol/g_{cat}$	Reduction degree(%)
CeO$_2$	0	39	18[a]
CeGd	1	37	20[a]
CeY	5	59	33[a]
CePr	38	57	57[a]
CeZr	36	60	56[a]
CeNb	12	68	44[a]
Ni/CeO$_2$	312	37	117[b]
Ni/CeGd	240	58	112[b]
Ni/CeY	225	10	104[b]
Ni/CePr	290	49	157[b]
Ni/CeZr	280	45	149[b]
Ni/CeNb	110	64	46[b]

[a] Reduction degree of CeO$_2$, calculated using the total amount of H_2 consumed.
[b] Reduction degree of NiO, calculated using the amount of H_2 consumed at low temperature region.

observed for Ni/CeGd, while Ni/CeZr exhibited the smallest Ni crystallite size.

The TEM images of the calcined and reduced Ni/CeGd and Ni/CeNb catalysts are shown in Figs. 5 and 6. The combined TEM and EDS analyses reveal that large NiO and Ni^0 particles are surrounded by smaller ceria particles, in good agreement with the crystallite size calculated by XRD.
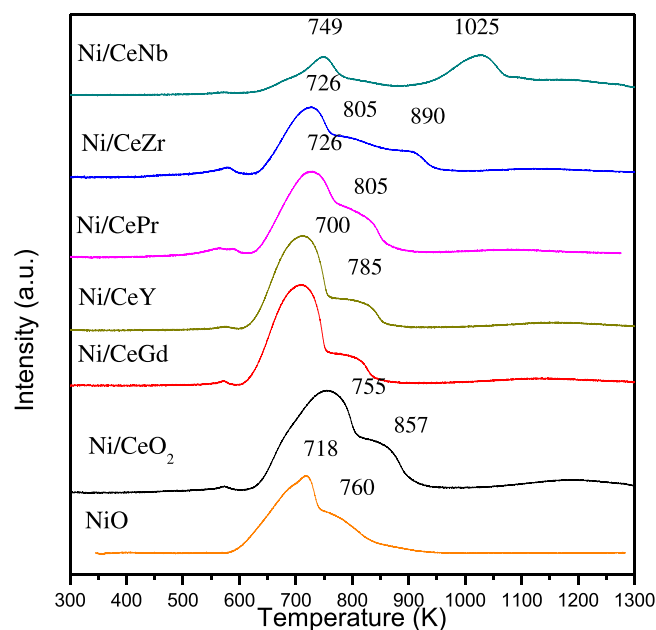
The TPR profile of ceria-based supports is displayed as supplementary data (Fig. S4 in the online version at DOI: http://dx.doi.org/10.1016/j.apcatb.2017.01.069). The reduction profile showed a peak at around 1160 K for all supports. CeO$_2$, CeGd and CeZr also exhibited a small H_2 consumption between 600 and 900 K. Two peaks at 805 and 855 K were also observed in the TPR profile of CePr. For CeNb, a small H_2 uptake was detected between 950 and 1050 K, and possibly associated with segregated Nb-rich phases. According to the literature [58,59], the TPR profile of CeO$_2$ generally exhibits two peaks. The first one at around 820 K is attributed to the surface reduction of CeO$_2$, and the second one at 1220 K is related to the reduction of bulk ceria and the formation of Ce$_2$O$_3$. When a dopant such as Zr was added to ceria structure, it was noticed an increase in the H_2 consumption at lower temperatures. This indicates that the dopant promotes the reduction of ceria due to an increase in oxygen mobility induced by the solid solution formation.

Therefore, in the present study, the H_2 uptake at low temperatures (600–900 K) was attributed to the surface reduction of CeO$_2$ and the peaks at higher temperatures (>900 K) were associated with the reduction of bulk ceria. In the case of CeNb, the H_2 consumption observed at 950 and 1050 K could also be ascribed to the reduction of the niobium oxide or cerium niobate [60].

A comparison between the H_2 consumption obtained for all supports showed that CePr and CeZr exhibited the highest reduction degree (Table 5). These results indicated that these samples showed the highest reducibility.

The TPR profile of Ni/CeO$_2$, Ni/CeGd, Ni/CeY, Ni/CePr and Ni/CeZr samples and the reference (NiO) were very similar (Fig. 7), showing a reduction peak at 700–755 K and a shoulder at 760–890 K. Comparing these results with the corresponding in situ X-rays diffractograms, the H_2 consumption between 700 and 890 K could be assigned to the reduction of NiO to Ni^0.

Roh et al. [61] and Augusto et al. [15] reported similar TPR profiles for bulk NiO and Ni supported on ceria-based oxides. According to these previous results, there is no strong interaction between NiO and CeO$_2$ due to the large crystallite sizes of both support and NiO phases formed at high calcination temperatures. Therefore, the TPR profiles obtained in this work suggest the formation of large NiO particles for Ni/CeO$_2$, Ni/CeGd, Ni/CeY, Ni/CePr and Ni/CeZr catalysts, which agrees with both XRD and TEM results.

Fig. 7. TPR profiles of calcined samples.

For Ni/CeO$_2$, Ni/CeGd, Ni/CeY, Ni/CePr and Ni/CeZr, the reduction degree of NiO was higher than 100% (Table 5). This effect was more significant for the samples containing Pr and Zr. Therefore, the H_2 consumption at low temperature region (600–900 K) observed for these catalysts could be associated with the reduction of bulk NiO as well as to the promoted reduction of CeO$_2$ by the metallic nickel particles formed. According to the literature [33,62] this promoting effect is due to the hydrogen spillover from the metal particles onto the support.

The TPR profile of Ni/CeNb catalyst is completely different from the ones obtained for the other catalysts. There are two small reduction peaks at 749 and 1025 K. Furthermore, the reduction degree of NiO for this sample was lower than 100% (46%). The first peak could be attributed to the NiO reduction and the second one could be related to the reduction of Ni species in interaction with the support. Comparing the TPR profile of Ni/CeNb with the one characteristic of bulk NiO shows that the addition of Nb did not promote the reduction of NiO particles. These results agree very well with the in situ XRD analyses and indicate that a Ni–Nb solid solution was not formed in significant extent on Ni/CeNb catalyst. The lower reducibility of Ni/CeNb sample has been attributed to the formation of a crystalline NiNb$_2$O$_6$ phase that is reduced at high temperature
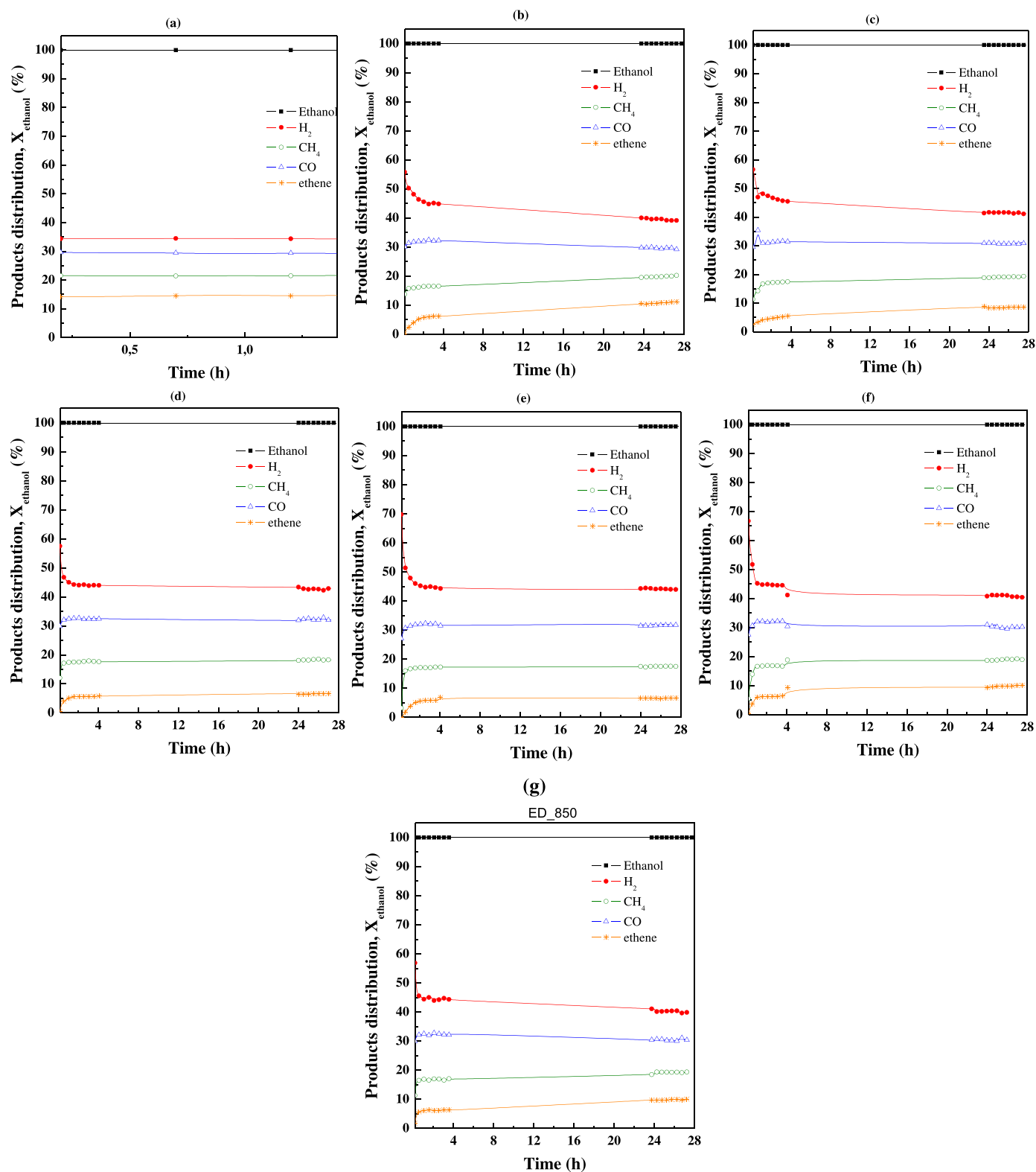
Fig. 8. Ethanol conversion and products distribution versus TOS for ED at 1123 K over (a) no catalyst, (b) Ni/CeO$_2$, (c) Ni/CeGd, (d) Ni/CeY, (e) Ni/CePr, (f) Ni/CeZr and (g) Ni/CeNb.

region (T > 773 K) in TPR analyses [49,53]. Therefore, in our work, the H$_2$ consumption at 1025 K is likely due to the reduction of a nickel niobate phase, which was not detected in the XRD analyses due to its low concentration.

3.2. Reactions

3.2.1. ED at 1123 K

Fig. 8 shows the ethanol conversion and product distributions as a function of time on stream (TOS) for ED at 1123 K over all catalysts and, as a reference, without catalyst. For the reaction without

catalyst, the initial conversion of ethanol was 100% and remained constant during reaction. The products observed were H_2, CO, CH_4 and ethylene. The reaction in the presence of the catalysts showed the formation of the same products but the selectivities to products were quite different from those obtained without catalyst. For instance, the initial selectivity to H_2 varied from 55 to 70% depending on the catalyst whereas it was only 35% for the reaction in gas phase. The same was observed for the initial selectivity to ethylene, which was zero for all catalysts and 15% for the reaction in gas phase. The deactivation of the catalysts led to a decrease in the selectivity to H_2 whereas the selectivity to ethylene increased. These results demonstrate that the reaction on the surface of the catalysts is the dominant reaction pathway. According to the previously proposed mechanism for the ethanol conversion reactions [32], ethanol is firstly dehydrogenated to acetaldehyde and H_2. Acetaldehyde can desorb in the gas phase and/or be decomposed in CH_4 and CO. Acetaldehyde can also react with hydroxyl groups to form the products of steam reforming of ethanol, H_2 and CO_2. Additionally, ethanol dehydration on the support may produce ethylene. In this study, the products formed indicate the occurrence of both decomposition and dehydration of ethanol reactions.

The formation of H_2 significantly decreased during the first hours of reaction, reaching values around 40–45% after 28 h of TOS for all catalysts. The decrease in H_2 production was followed by an increase in CO, CH_4 and ethylene formation. After 28 h of TOS, the selectivities to CO, CH_4 and ethylene were around 30, 20 and 5–10%, respectively, regardless of catalyst composition.

Augusto et al. [15,31] reported the same result for ED over Ni/CeGd catalyst. The characterization of used catalysts by SEM and TG analyses revealed the formation of carbon on the catalyst, which was responsible for catalyst deactivation.

For catalysts working on SOFC operating conditions (high reaction temperatures), carbon formation is a critical issue. Laosiripojana and Assabumrungrat [1] studied the performance of 39 wt.% Ni/YSZ as anode for bio-ethanol fueled SOFC. Large amounts of carbon deposits were formed during SR of ethanol in the temperature range of 1173–1273 K. Carbon formation was attributed to the decomposition of hydrocarbons (methane, ethane and ethylene) as well as the Boudouard reaction.

In the present study, in situ XRD under reaction conditions, SEM and TG analyses of the used catalysts were carried out to investigate possible causes for catalyst deactivation during ED at 1123 K and the results will be discussed in the next section.

3.3. Catalyst deactivation

Figs. 9–11 show the in situ XRD patterns obtained during ED at 1123 K over Ni/CeO$_2$, Ni/CeGd and Ni/CeNb catalysts. The diffractograms of the other ceria-doped samples are presented in the supplementary information (Figs. S5–S7 in the online version at DOI: http://dx.doi.org/10.1016/j.apcatb.2017.01.069). The diffractograms of all catalysts reduced at 1123 K under H_2 for 30 min exhibited the lines of partially reduced ceria (CeO$_x$) and Ni^0. After 3 min of reaction, the lines corresponding to CeO$_x$ remained unchanged for all catalysts. After this period, no significant changes were detected in the CeO$_x$ lines for Ni/CeO$_2$. On the other hand, for ceria-doped catalysts, the diffraction lines of CeO$_x$ phase significantly shifted to lower 2θ position during the reaction. This shift increased in the following order: Ni/CeNb < Ni/CeZr < Ni/CeGd < Ni/CePr < Ni/CeY. This result indicates that both ceria and Ce$_{1-x}$Ni$_x$O$_{2-y}$ mixed-oxides were further reduced by H_2 and CO produced during the reaction, and oxygen vacancies were created, mainly for samples containing Y and Pr. Furthermore, the lines of NiO were not detected during the reaction, indicating that there was no oxidation of Ni^0 crystallites. Table 6 presents the lattice parameter during the reaction.
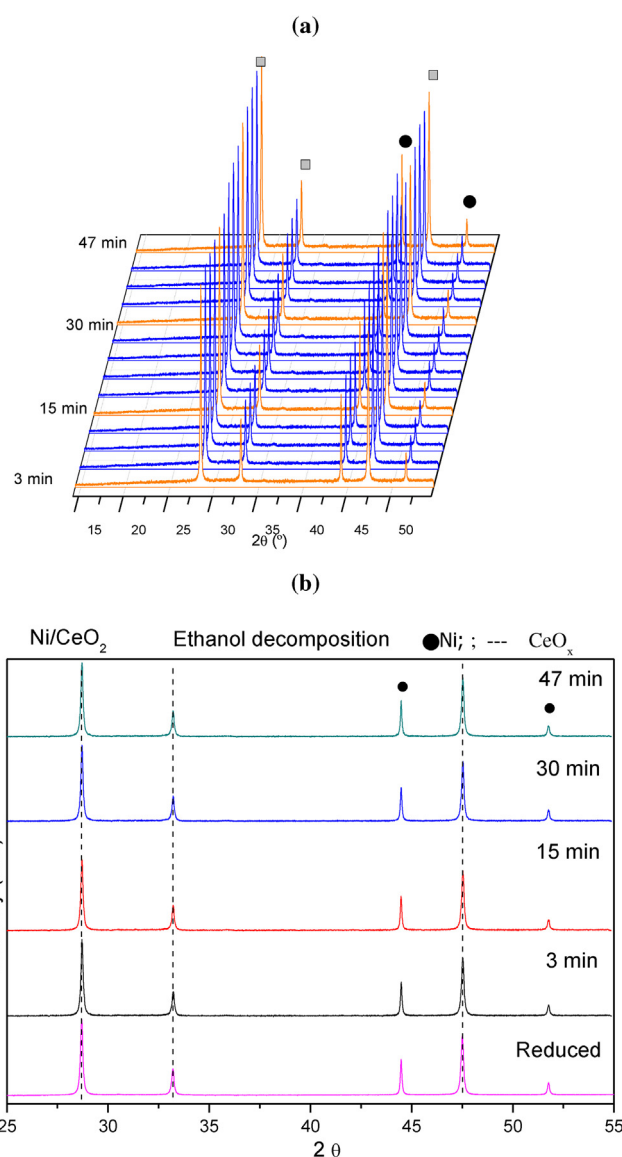

(a)

(b)

Fig. 9. X-ray diffraction patterns obtained for Ni/CeO$_2$ (orange curves) during (a) ED reaction during 1 h TOS at 1123 K (b) (orange curves) selected times (orange curves). (—) CeO$_x$; (●) Ni. (For interpretation of the references to colour in this figure legend, the reader is referred to the web version of this article.)

Table 6
Lattice parameter of CeO$_2$ during reaction at different TOS.

Sample	Lattice parameter (A)			
	3 min reaction	15 min reaction	30 min reaction	60 min reaction
Ni/CeO$_2$	5.4622	5.4630	5.4637	5.4711
Ni/CeGd	5.4566	5.4870	5.5075	5.5233
Ni/CeY	5.4603	5.5116	5.5164	5.5466
Ni/CePr	5.5100	5.5327	5.5465	5.5922
Ni/CeZr	5.4641	5.4955	5.5098	5.5254
Ni/CeNb	5.4717	5.4836	5.4902	5.4936

All samples showed a continuous expansion of the lattice parameter with increasing reaction time due the reduction of Ce^{+4} to Ce^{+3} as previously discussed.

A comparison between the samples reduced at 1123 K and after reaction showed a slight increase in CeO$_2$ crystallite sizes for Ni/CeGd and Ni/CePr during 1 h of TOS (Table 3). However, CeO$_2$ crystallite sizes remained unchanged for the other samples. Fur-
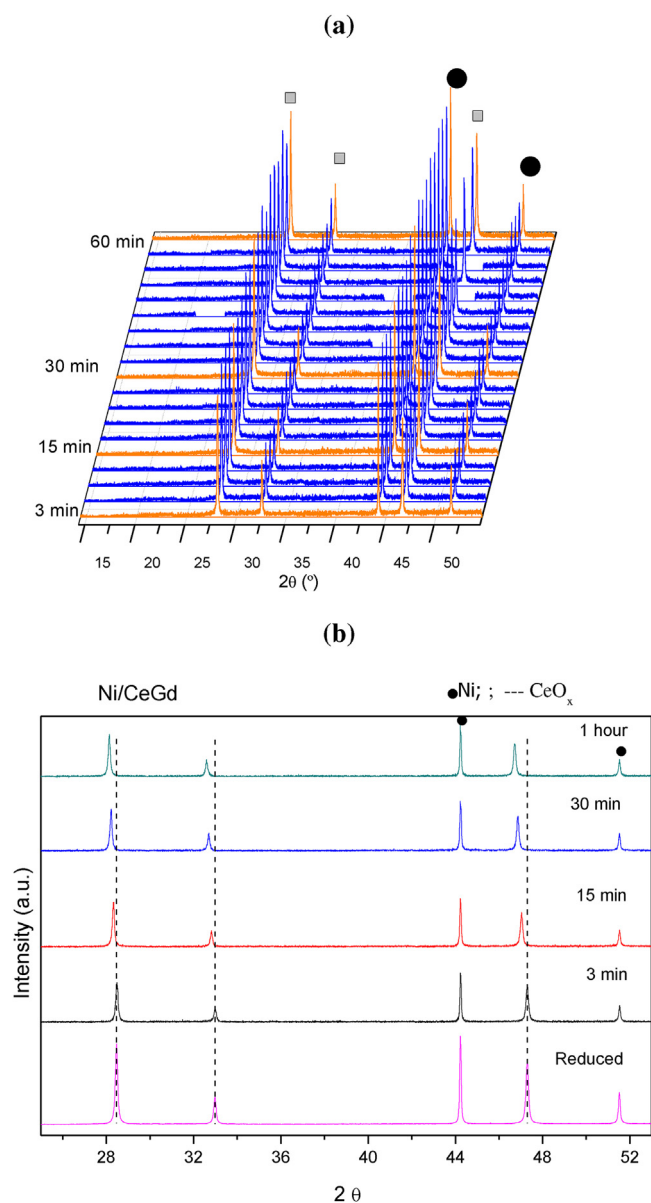
(a)

(a)

(b)

(b)

Fig. 10. X-ray diffraction patterns obtained for Ni/CeGd during (a) ED reaction during 1 (orange curves) h TOS at 1123 K (b) (orange curves) selected times (orange curves). (−) CeO$_x$; (●) Ni. (For interpretation of the references to colour in this figure legend, the reader is referred to the web version of this article.)

Fig. 11. X-ray diffraction patterns obtained for Ni/CeNb during (a) ED reaction during 1 h TOS at 1123 K (b) Selected times (orange curves). (−) CeO$_x$; (●) Ni. (For interpretation of the references to colour in this figure legend, the reader is referred to the web version of this article.).

thermore, the Ni^0 crystallite sizes slightly increased during the reaction, except for Ni/CeO$_2$ and Ni/CeNb (Table 4).

SEM micrographs of the Ni-based catalysts after ED at 1123 K are shown in Fig. 12. Carbon filaments were observed for all catalysts. Ni/CeZr and Ni/CeGd samples showed the highest amount of carbon filaments.

The TPO profiles of used Ni-based catalysts after ED at 1123 K are shown in Fig. 13. All catalysts exhibited only one peak at around 910–923 K, except for Ni/CeGd that showed a pronounced peak at 895 K and a shoulder at 923 K. TPO experiments have been extensively used to study the nature of the carbonaceous deposits and the amount of carbon formed over supported Ni catalysts after ethanol conversion reactions [63–67]. According to previous studies, the peaks in the low temperature region of the TPO profile (<673 K) correspond to the oxidation of amorphous carbon overlaying the metal surface. The peaks at high temperatures were due to the oxidation of filamentous (773–873 K) and graphitic carbon (>873 K).
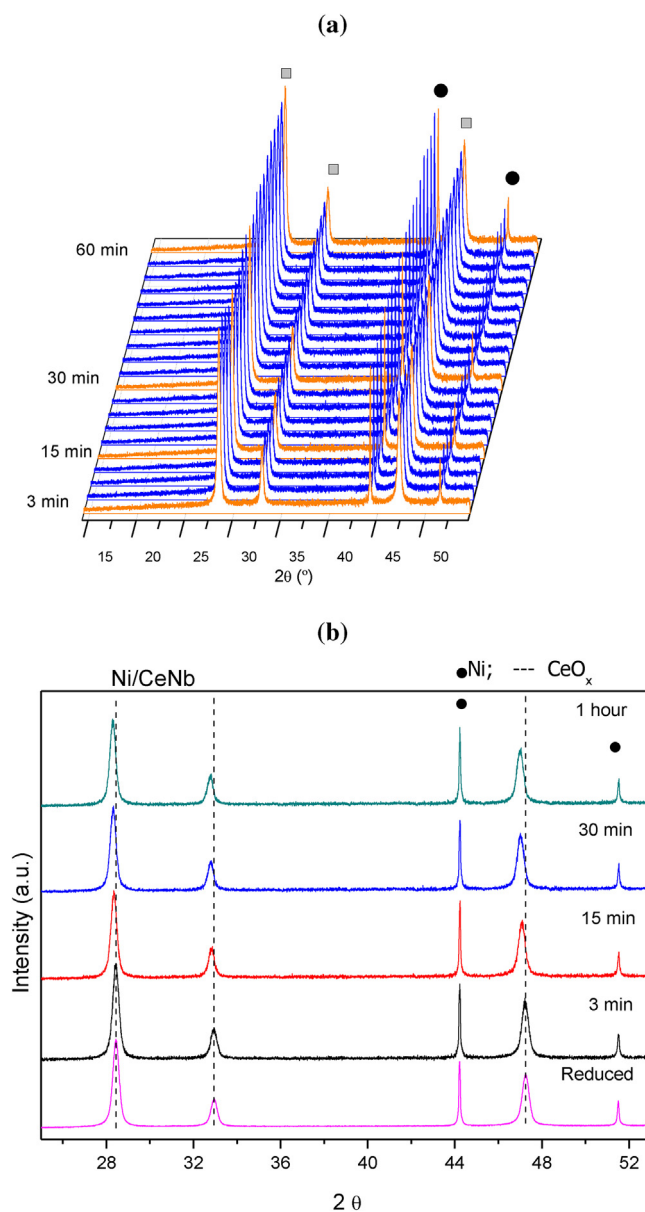
Augusto et al. [31] investigated the effect of calcination temperature of Ni/CeGd catalyst and of reaction temperature on ethanol conversion reactions. TPO profiles of Ni/CeGd catalysts after steam reforming of ethanol and ethanol decomposition at 773 K exhibited peaks in the temperature range of 860–895 K, regardless of the catalyst calcination temperature. Increasing the reaction temperature (1073 K), only a peak at 950 K was detected on the TPO profile of Ni/CeGd catalyst after ethanol decomposition reaction. These peaks were assigned to the oxidation of filamentous and graphitic carbon, respectively, similarly to the results shown in Fig. 13.

The amount of carbon deposited on Ni-based catalysts after ED at 1123 K are listed in Table 7. Ni/CeGd exhibited the highest amount of carbon deposits (11.6 mg$_{carbon}$/g$_{cat}$/h), whereas the lowest quantity of carbon was detected over Ni/CeNb catalyst (1.5 mg$_{carbon}$/g$_{cat}$/h). The other samples presented comparable amounts of carbon (5–8 mg$_{carbon}$/g$_{cat}$/h).
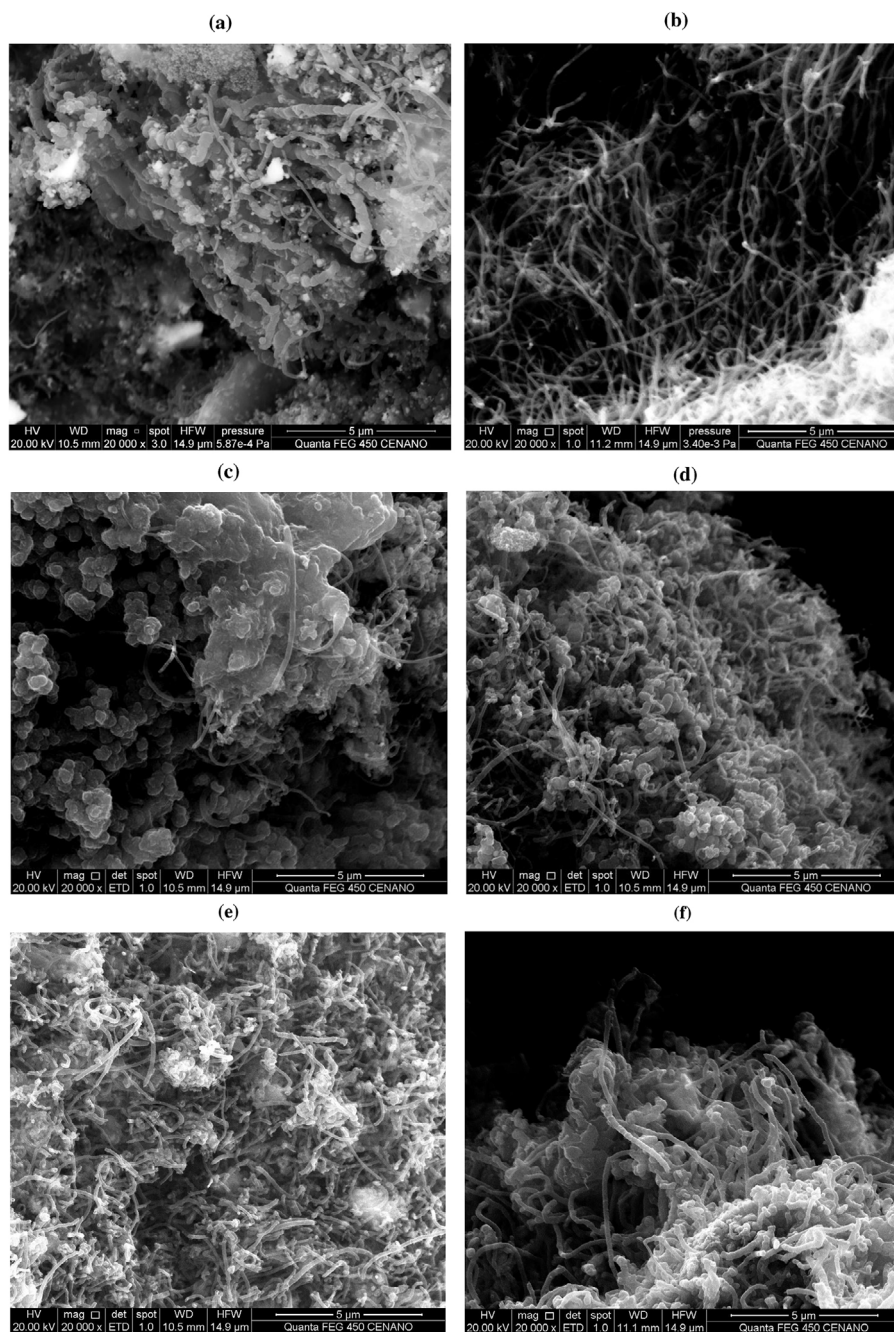
Fig. 12. SEM images of used catalysts after ED reaction at 1123 K. (a) Ni/CeO$_2$; (b) Ni/CeGd; (c) Ni/CeY; (d) Ni/CePr; (e) Ni/CeZr; (f) Ni/CeNb.

Table 7
Amount of carbon deposited on Ni-based catalysts after ED at 1123 K (mg$_{carbon}$/(g$_{cat}$.h)).

Sample	Amount of carbon (mg$_{carbon}$/(g$_{cat}$ h))
Ni/CeO$_2$	5.9
Ni/CeGd	11.6
Ni/CeY	5.1
Ni/CePr	6.0
Ni/CeZr	7.8
Ni/CeNb	1.5

Therefore, carbon deposition was the main reason for catalyst deactivation in the present work. The main reactions that contribute to coke formation during ethanol conversion are as follows: (i) ethanol dehydration to ethylene, followed by polymerization to coke; (ii) aldol condensation of acetone followed by dehydration to mesityl oxide (MO); (iii) the Boudouard reaction; (iv) the reverse of carbon gasification; and (v) the decomposition of hydrocarbons such as methane and ethylene [32]. The extent of each reaction depends on both reaction conditions and the catalyst used. The decomposition of methane and ethylene to H$_2$ and C are the main reactions for carbon deposition under the reaction conditions used in our work, which are typical of SOFC operation (high reaction temperature: 1123 K). Despite the formation of methane and ethylene over all catalysts, carbon formation was markedly lower on Ni/CeNb catalyst.

The oxygen mobility that could be at the origin of the difference in the amount of carbon deposition was evaluated by the oxygen isotopic exchange technique. The study was limited to CeGd, CeNb, which displayed the largest difference of carbon deposited,
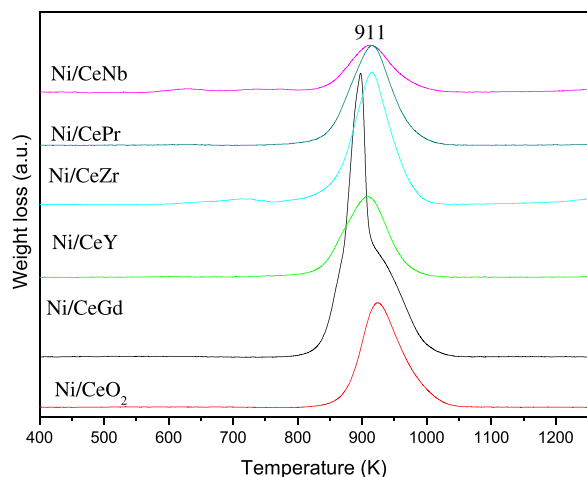
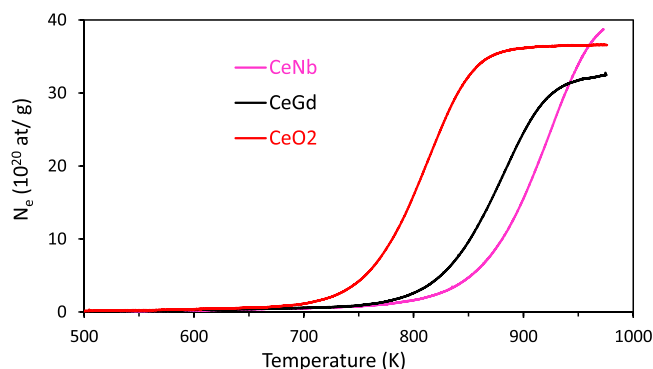**Fig. 13.** TPO profiles of used Ni–based catalysts after ED at 1123 K.

Fig. 14. Evolution of the number of exchanged oxygen atoms during temperature-programmed heterolytic $^{18}O_2/^{16}O_2$ exchange over CeO_2, CeNb and CeGd after oxidizing pre-treatments of the samples.

Fig. 15. Evolution of the number of exchanged oxygen atoms during isothermal heterolytic $^{18}O_2/^{16}O_2$ exchange over CeO_2, CeNb and CeGd at (a) 780 K and (b) 878 K after oxidizing pre-treatments of the samples.

Table 8
Initial rate of exchange, R_e, calculated from IOIE experiments at 780 and 878 K (10^{20} at/(gcat min)).

Sample	R_e at 780 K (10^{20} at/($gcat_{cat}$ min))cat	R_e at 878 K (10^{20} at/($gcat_{cat}$ min))cat
CeO_2	0.97	9.12
CeGd	0.66	6.64
CeNb	0.10	0.73

and CeO_2 support to evaluate the influence of dopants. A first set of experiments was performed in temperature-programmed conditions. To prevent the reoxidation of the samples when introducing the labelled oxygen molecule, the experiments have been performed on pre-oxidized supports. The time dependence of the partial pressures of each isotope during the TPOIE experiments over the three samples are shown in Fig. S8 in the online version at DOI: http://dx.doi.org/10.1016/j.apcatb.2017.01.069. The CeO_2 started to exchange with $^{18}O_2$ above 700 K, which was higher than the previously reported temperature (583 K) [38]. At low temperature, the specific surface area influences the exchange activity. This result confirms the effect of the high temperature of calcination used for SOFC application. At the beginning of the reaction, both isotopomers, $^{16}O_2$ and $^{16}O^{18}O$, were formed, indicating that both simple and multiple heterolytic exchange mechanisms were involved, as previously reported for CeO_2. The addition of Gd and Nb to ceria did not decrease the temperature of exchange. On the contrary, a shift to higher temperatures was observed for CeGd and CeNb. For an easiest comparison, the time dependence of the number of exchanged atoms (N_e) calculated for each support are shown in Fig. 14. The negative impact was more pronounced for the CeNb support since the plateau that corresponds to the equilibrium of ^{18}O concentration between the gas phase and the solid surface was not reached at 973 K. The isotopic distribution for CeNb (Fig. S8b) with the appearance in the gas phase of the $^{16}O_2$ isotope at the initial time of exchange suggests a higher concentration of deficient oxygen sites on the ceria surface due to the addition of Nb. These sites are known to activate the oxygen in the diatomic form and favor
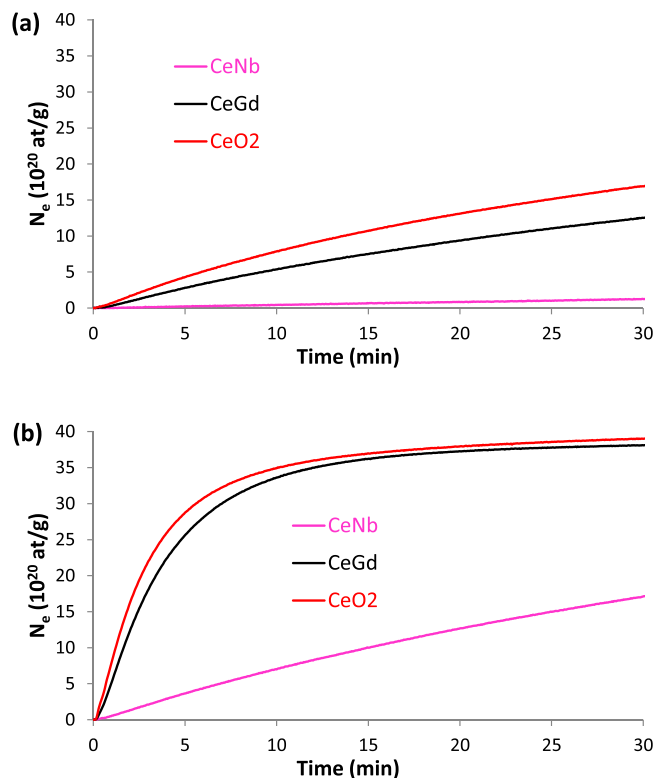
the multiple exchange mechanism. However, such an effect did not result in lower temperature of exchange in the present study.

The experiments performed in isothermal conditions confirmed such a behavior. The isotopic distributions during the exchange reaction at 780 and 878 K are shown in Figs. S9 and S10 in the online version at DOI: http://dx.doi.org/10.1016/j.apcatb.2017.01.069, respectively, while the evolution of the N_e values are compared in Fig. 15. The difference of activity is less visible between CeO_2 and CeGd than for TPOIE experiments, but a higher activity in exchange is still observed for pure CeO_2. The initial rate of exchange (R_e) was calculated for each experiment and the obtained values are listed in Table 8. At 780 K, the rates of exchange were 0.97, 0.66 and 0.1×10^{20} oxygen atoms/(g_{cat} min) for CeO_2, CeGd and CeNb, respectively. The rate of exchange increased with temperature, as expected. At 878 K, the R_e values were 9.12, 6.64 and 0.73×10^{20} oxygen atoms/(g_{cat} min) for CeO_2, CeGd and CeNb, respectively. The lowest activity of CeNb was clearly evidenced as well as the difference in the exchange mechanism over CeNb support with the preponderance of the $^{16}O_2$ isotope during the exchange reaction.

3.4. Discussion

The development of anodes for direct ethanol SOFCs showing high stability and adequate ionic and electronic conductivity at

working conditions is one of the main issues for the commercialization of this technology [7,8]. The use of ceria as support has been proposed to improve catalyst resistance to carbon deposition. Ceria exhibits a mixed ionic-electronic conductivity, adequate to SOFC and a high oxygen mobility that assists on the removal of carbon, improving catalyst stability [68].

Laosiripojana et al. [1] suggested that the high resistance to carbon deposition for Ni supported over a high surface area ceria catalyst during SR of ethanol at high temperature (973–1273 K) was due to the high oxygen storage capacity (OSC) of ceria. At high temperature, the reaction rate between the lattice oxygen of the support and carbon formed is improved, resulting in the removal of carbon.
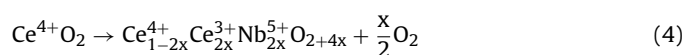
According to the literature [33], doping of ceria with cations such as Gd^{3+}, Y^{3+}, Pr^{3+} and Zr^{4+} should enhance the mobility of oxygen in ceria and then, increase the OSC of the support. Therefore, these materials should exhibit a higher resistance to carbon formation during ED than Ni/CeO_2 catalyst. In fact, TPR and in situ XRD showed a higher reducibility of Zr and Pr doped ceria, in accordance with previous reports. However, the amount of carbon deposited on these materials was like that one formed over Ni/CeO_2 catalyst. This result suggests that the mechanism of carbon removal is not effective under the ED reaction conditions at high temperature. This mechanism is based on the oxygen transfer from the support to the surface of the metal particle, which contributes to the removal of carbon from the metal. This reaction is believed to occur at the metal–support interfacial perimeter. Therefore, the maintenance of a high metal-support interfacial area is crucial for an efficient cleaning of the metal particle.

In the present study, the in situ XRD experiments and TEM images revealed the presence of large Ni^0 particles after reduction for all samples. In addition, it was observed an increase in Ni^0 crystallite sizes for Ni/CeY and Ni/CePr catalysts during ED reaction. Ni/CeGd exhibited the largest Ni crystallite size as well as the amount of carbon deposited.

The particle size of metal affects significantly the carbon formation over metallic nickel particles. The initiation step for carbon formation over metal particle is favored for larger crystallite sizes. Recently, the effect of Co particle size on the performance of carbon nanofiber supported Co catalysts for SR of ethanol was also investigated [27]. It was found a decrease in deactivation rate with decreasing cobalt particle size. The lower carbon deposition rate was ascribed to a lower fraction of exposed terrace atoms, in which carbon deposition on catalysts with large metallic particles is initiated.

For large particles, the initiation step for carbon formation is favored and the metal-support interface is low, which reduces the efficiency of the cleaning mechanism by the support. Therefore, the effectiveness of doping ceria to inhibit carbon formation is low when the material is processed in similar conditions to those used for SOFC fabrication. Thus, the high temperature of sintering required for the preparation of anodes result in large Ni particles even for low Ni loading.

However, Ni/CeNb catalyst exhibited the lowest amount of carbon deposits, suggesting that niobia-doped ceria reduced the formation of carbon. The doping of ceria with elements of valence higher than 4+, such as Nb^{5+} leads either to the incorporation of the excess oxygen as interstitials (Eq. (3)) or to an electronic compensation leading to cerium reduction (Eq. (4)).

$$Ce^{4+}O_2 \rightarrow Ce^{4+}Nb_{2x}^{5+}O_{2+5x} \tag{3}$$

$$Ce^{4+}O_2 \rightarrow Ce_{1-2x}^{4+}Ce_{2x}^{3+}Nb_{2x}^{5+}O_{2+4x} + \frac{x}{2}O_2 \tag{4}$$

However, the solubility of niobium oxide in ceria is low (1.4% mole fraction) [43,68] but it could increase under reducing conditions. In fact, in situ XRD experiments revealed that the shift of the

ceria lines to lower 2θ positions for Ni/CeNb was less pronounced than that for Ni/CeZr and Ni/CePr. Therefore, the formation of oxygen vacancies could not explain the highest resistance to carbon formation of Ni/niobia-doped ceria catalyst.

The TPR experiment showed that Ni/CeNb sample had the lowest reducibility, with a reduction degree of NiO of only 46%, while all remaining samples exhibited complete reduction of nickel oxide. The oxygen isotopic exchange experiments also demonstrated the low oxygen mobility in the CeNb support compared with pure CeO_2.

Hu et al. [69,70] studied the effect of the calcination temperature on the extent of $Rh-Nb_2O_5$ interaction on the niobia-promoted Rh/SiO_2 catalyst. Increasing the calcination temperature favored the formation of $RhNbO_4$ compound, which is reduced at high temperature during TPR. The reduction at high temperature led to the suppression of H_2 chemisorption and ethane hydrogenolysis activity. They proposed that $RhNbO_4$ is reduced to Rh and NbO_2 species that decorates the surface of Rh particles, decreasing the reaction rate for ethane hydrogenolysis.

Our results suggest the formation of a nickel niobate phase during calcination at high temperature. The reduction of this niobium-rich phase could lead to the formation of Ni particles covered by NbO_x patches. The presence of these species on the surface of metallic particles would block active sites, preferentially affecting those reactions that require a large ensemble of atoms. According to Rostrup-Nielsen [71], there is a critical ensemble size for steam reforming (3–4 nickel atoms) while the formation of carbon requires larger ensembles (6–7 atoms). Therefore, carbon formation is inhibited while maintaining some activity for reforming reaction on Ni particles covered by NbO_x species, the so-called geometric effect [72].

In order to understand the highest resistance to carbon formation of Ni/CeNb catalyst, two catalysts containing this phase supported on ceria ($NiNb_2O_6/CeO_2$ samples calcined at 1073 K and 1273 K) were prepared as described in the experimental session.

Fig. 16 shows the XRD patterns of the $NiNb_2O_6/CeO_2$ samples calcined at 1073 K and 1273 K. The diffractogram of the sample calcined at 1073 K exhibited the lines characteristic of CeO_2 with cubic structure (ICSD 72155), NiO (JCPDS 24018), $NiNb_2O_6$ (PDF32-0694) and Nb_2O_5 (PDF 43-1042) phases. The calcination at 1273 K led to the disappearance of the lines assigned to Nb_2O_5 phase and to the increase in the intensity of the lines attributed to $NiNb_2O_6$ phase. According to the literature, the calcination at high temperature induces the reaction between Nb_2O_5 and NiO, leading to the formation of $NiNb_2O_6$ [73]. Therefore, the sample calcined at higher temperature has a higher fraction of $NiNb_2O_6$. It was also noticed the lines corresponding to $CeNbO_4$ (PDF 72-0905), as a minor secondary phase.

The TPR profiles of both samples are shown in Fig. S11 in the online version at DOI: http://dx.doi.org/10.1016/j.apcatb.2017.01.069. For $NiNb_2O_6/CeO_2$ sample calcined at 1073 K, one peak at 760 K and two small peaks at high temperature can be identified. Based on the XRD data, the peak at low temperature could be attributed to the reduction of NiO particles, whereas the hydrogen uptake at high temperature is likely due to the reduction of $NiNb_2O_6$ phase. The calcination at high temperature decreased the intensity of the peak attributed to NiO and increased the hydrogen consumption at high temperature. Therefore, the calcination at 1273 K favored the formation of $NiNb_2O_6$ phase. Furthermore, the TPR profile of the Ni/CeNb is quite similar to the one of $NiNb_2O_6/CeO_2$ sample calcined at 1273 K, indicating that Ni/CeNb catalyst contains mainly the $NiNb_2O_6$ phase.

Fig. S12 in the online version at DOI: http://dx.doi.org/10.1016/j.apcatb.2017.01.069 shows the ethanol conversion and product distributions as a function of TOS for ED at 1123 K over both $NiNb_2O_6/CeO_2$ samples calcined at 1073 K and 1273 K. The initial conversion of ethanol was 100% and remained constant during 28 h
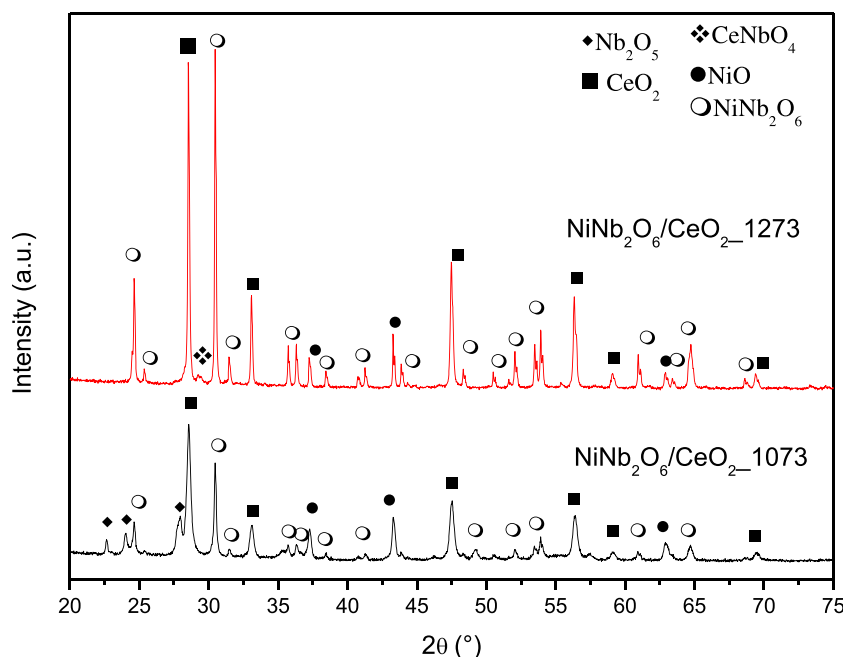
Fig. 16. X-ray diffraction patterns obtained for $NiNb_2O_6/CeO_2$ calcined at 1073 K and 1273 K.

of TOS, regardless of catalyst composition. The products observed for both catalysts were H_2, CO, CH_4 and small amounts of ethylene.

The formation of H_2 only slightly decreased during the first hours of reaction, reaching values around 45–48% after 28 h of TOS for both catalysts. The decrease in H_2 production was followed by a slight increase in CO, CH_4 and ethylene formation. After 28 h of TOS, the selectivity to CO, CH_4 and ethylene were around 32, 15–16 and 7%, respectively.

The TPO profiles of used samples after ED at 1123 K are shown in Fig. S13 in the online version at DOI: http://dx.doi.org/10.1016/j.apcatb.2017.01.069. Both samples exhibited a peak at 974 K, which corresponds to the formation of filamentous and graphitic carbon. The amount of carbon deposited on both samples after ED at 1123 K was 3.9 $mg_{carbon}/(g_{cat}$ h) for $NiNb_2O_6/CeO_2$ calcined at 1073 K and 4.4 $mg_{carbon}/(g_{cat}$ h) for $NiNb_2O_6/CeO_2$ calcined at 1273 K. These values were close to the ones obtained for the Ni/NbCe, suggesting that the formation of the $NiNb_2O_6$ phase inhibits carbon formation during ED at 1123 K.

4. Conclusions

Ni-based catalysts supported on CeO_2 doped with different cations (Gd, Y, Pr, Zr, Nb) were prepared by the hydrothermal method. The diffractograms of the calcined samples revealed the shift of CeO_2 diffraction lines for Ni/CeGd, Ni/CeY, Ni/CePr, Ni/CeZr and Ni/CeNb, which was due to the formation of solid solutions during calcination. In situ X-ray diffraction patterns obtained during reduction showed that CeO_2 diffractions lines shifted to lower 2θ positions as the temperature increased, which is related to the partial reduction of CeO_2 to CeO_x, with formation of Ce^{3+} cations and oxygen vacancies. The extent of ceria reduction depended on the type of dopant and followed the order Ni/CeGd < Ni/CeY < Ni/CeO$_2$ < Ni/CeNb < Ni/CeZr < Ni/CePr. The increase in the reduction temperature also significantly increased the Ni^0 crystallite size for all catalysts. The reduction was also monitored by TPR technique. The TPR profile of Ni/CeO$_2$, Ni/CeGd, Ni/CeY, Ni/CePr and Ni/CeZr samples corresponds to the reduction of large NiO particles without interaction with the large CeO_2 crystallites. However, the TPR profile of Ni/CeNb catalyst is

completely different from the ones obtained for the other catalysts. The hydrogen consumption at high temperature is attributed to the reduction of a $NiNb_2O_6$ phase.

These catalysts were tested for ED at 1123 K. H_2, CO, CH_4 and ethylene were the main products formed, indicating that ethanol decomposition and dehydration of ethanol are the main reactions taking place. However, the formation of H_2 significantly decreased during the first hours of reaction for all catalysts. SEM and TG analysis of the used catalysts revealed that carbon formation was the main cause of catalyst deactivation. The highest formation of carbon occurred over Ni/CeGd, whereas the lowest amount of carbon deposits was obtained on Ni/CeNb catalyst. The amount of carbon formed on Ni/CeO$_2$, Ni/CeY, Ni/CePr and Ni/CeZr catalysts was approximately the same. These results suggest that doping ceria with cations such as Gd^{3+}, Y^{3+}, Pr^{3+} and Zr^{4+} did not improve the resistance to carbon formation in spite of the higher oxygen mobility of doped-ceria supports. In fact, the calcination at high temperature significantly increased the Ni^0 and CeO_2 crystallite size, strongly decreasing the metal-support interfacial area. Therefore, the mechanism of carbon removal based on oxygen transfer from the support to the surface of the metal particle does not take place and then, carbon species accumulates leading to catalyst deactivation. In spite of several studies have proposed the use of redox supports to assist in carbon removal, this approach is not effective for SOFC anodes due to the typical operation conditions. The lowest formation of carbon on Ni/CeNb catalyst is likely due to presence of $NiNb_2O_6$ phase. The reduction of this phase could lead to the formation of Ni particles covered by NbO_x patches. The dilution or the coverage of a fraction of the surface of metallic particles by NbO_x species inhibits the formation of carbon by the so-called geometric effect.

References

[1] N. Laosiripojana, S. Assabumrungrat, J. Power Sources 163 (2007) 943–951.
[2] S.L. Douvartzides, F.A. Coutelieris, A.K. Demin, P.E. Tsiakaras, Int. J. Hydrogen Energy 29 (2004) 375–379.
[3] A. Arpornwichanop, N. Chalermpanchai, Y. Patcharavorachot, S. Assabumrungrat, M. Tade, Int. J. Hydrogen Energy 34 (2009) 7780–7788.
[4] N.Q. Minh, J. Am. Ceram. Soc. 76 (1993) 563–588.
[5] A. Atkinson, S. Barnett, R.J. Gorte, J.T.S. Irvine, A.J. Mcevoy, M. Mogensen, S.C. Singhal, J. Vohs, Nat. Mater. 3 (2004) 17–27.
[6] S. Park, J.M. Vohs, R.J. Gorte, Nature 404 (2000) 265–267.
[7] B.S. Prakash, S.S. Kumar, S.T. Aruna, Renew. Sustain. Energy Rev. 36 (2014) 149–179.
[8] A.S. Ferlauto, D.Z. De Florio, F.C. Fonseca, V. Esposito, R. Muccillo, E. Traversa, L.O. Ladeira, Appl. Phys. A 84 (2006) 271–276.
[9] E.N. Armstrong, J. Park, N.Q. Minh, Electrochem. Solid-State Lett. 15 (2012) B75–B77.
[10] R. Muccillo, E.N.S. Muccillo, F.C. Fonseca, D.Z. de Florio, J. Electrochem. Soc. 155 (2008) B232–B235.
[11] M. Cimenti, J.M. Hill, J. Power Sources 195 (2010) 3996–4001.
[12] S.P. Jiang, Y. Ye, T. He, S.B. Ho, J. Power Sources 185 (2008) 179–182.
[13] S.D. Nobrega, M.V. Galesco, K. Girona, D.Z. Florio, M.C. Steil, S. Georges, F.C. Fonseca, J. Power Sources 213 (2012) 156–159.
[14] S.D. Nobrega, P. Gelin, S. Georges, M.C. Steil, B.L. Augusto, F.B. Noronha, F.C. Fonseca, J. Electrochem. Soc. 161 (2014) F354–F359.
[15] B.L. Augusto, F.B. Noronha, F.C. Fonseca, F.N. Tabuti, R.C. Colman, L.V. Mattos, Int. J. Hydrogen Energy 39 (2014) 11196–11209.
[16] Z. Tao, G. Hou, N. Xu, Q. Zhang, Int. J. Hydrogen Energy 39 (2014) 5113–5120.
[17] B. Farrell, S. Linic, Appl. Catal. B: Environ. 183 (2016) 386–393.
[18] S.D. Nobrega, M.C. Steil, S. Georges, S. Uhlenbruck, F.C. Fonseca, ECS Trans. 68 (2015) 2851–2858.
[19] Y. Jiang, Y.A. Virkar, J. Electrochem. Soc. 148 (2001) A706–709.
[20] W.F. Ye, B. Huang, S.R. Wang, T.L. Xiong, J. Power Sources 164 (2007) 203–209.
[21] X.F. Ye, S.R. Wang, Z.R. Wang, T.L. Xiong, X.F. Sun, T.L. Wen, J. Power Sources 177 (2008) 419–425.
[22] X.F. Ye, S.R. Wang, Q. Hu, J.Y. Chen, T.L. Wen, Z.Y. Wen, Solid State Ion. 180 (2009) 276–281.
[23] B. Huang, S.R. Wang, R.Z. Liu, T.L. Wen, J. Power Sources 167 (2007) 288–294.
[24] B. Huang, S.R. Wang, R.Z. Liu, X.F. Ye, H.W. Sun, T.L. Wen, J. Power Sources 167 (2007) 39–46.
[25] B. Huang, X.J. Zhu, W.Q. Hu, Y.Y. Wang, Q.C. Yu, J. Power Sources 195 (2010) 3053–3059.
[26] W. Wang, C. Su, T. Zheng, M. Liao, Z. Shao, Int. J. Hydrogen Energy 37 (2012) 8603–8612.
[27] A.L.M. da Silva, J.P. den Breejen, L.V. Mattos, J.H. Bitter, K.P. de Jong, F.B. Noronha, J. Catal. 318 (2014) 67–74.
[28] J.R. Rostrup-Nielsen, J. Sehested, J. Norskov, Adv. Catal. 47 (2002) 65–139.
[29] V. Modafferi, G. Panzera, V. Baglio, F. Frusteri, P.L. Antonucci, Appl. Catal. A: Gen. 334 (2008) 1–9.
[30] P. Jasinski, T. Suzuki, V. Petrovsky, H.U. Anderson, Electrochem. Solid-State Lett. 8 (2005) A219–A221.
[31] B.L. Augusto, L.O.O. Costa, F.B. Noronha, R.C. Colman, L.V. Mattos, Int. J. Hydrogen Energy 37 (2012) 12258–12270.
[32] L.V. Mattos, G. Jacobs, B.H. Davis, F.B. Noronha, Chem. Rev. 112 (2012) 4094–4123.
[33] J. Kašpar, P. Fornasiero, M. Grazian, Catal. Today 50 (1999) 285–298.
[34] H. Inaba, H. Tagawa, Solid States Ion. 83 (1996) 1–16.
[35] H. Yashiro, Y. Eguchi, K. Eguchi, H. Arai, J. Appl. Electrochem. 18 (1988) 527–531.
[36] C. Ftikos, M. Nauer, B.C.H. Steele, J. Eur. Ceram. Soc. 12 (1993) 267–270.
[37] E. Heracleous, A.A. Lemonidou, J. Catal. 270 (2010) 67–75.
[38] Y. Madier, C. Descorme, A.M. Le Govic, D. Duprez, J. Phys. Chem. B 103 (1999) 10999–11006.
[39] D. Martin, D. Duprez, J. Phys. Chem. 100 (1996) 9426.
[40] F.B. Passos, E.R. de Oliveira, L.V. Mattos, F.B. Noronha, Catal. Today 101 (2005) 23–30.
[41] D. Terribile, A. Trovarelli, J. Llorca, C. de Leitenburg, G. Dolcetti, Catal. Today 43 (1998) 79–88.
[42] C.E. Hori, H. Permana, K.Y.S. Ng, A. Brenner, K. More, K.M. Rahmoeller, D. Belton, Appl. Catal. B: Environ. 16 (1998) 105–117.
[43] E. Ramírez-Cabrera, N. Laosiripojana, A. Atkinson, D. Chadwick, Catal. Today 78 (2003) 433–438.
[44] H. Li, G. Lu, Y. Wang, Y. Guo, Y. Guo, Catal. Commun. 11 (2010) 946–950.
[45] M.D. Salazar-Villalpando, B. Reyes, Int. J. Hydrogen Energy 34 (2009) 9723–9729.
[46] A. Bonk, A. Remhof, A.C. Maier, M. Trottmann, M.V.F. Schlup, C. Battaglia, U.F. Vogt, J. Phys. Chem. C 120 (2016) 118–125.
[47] M. Yashima, T. Takizawa, J. Phys. Chem. C 114 (2010) 2385–2392.
[48] J.B. Wang, Y. Tai, W. Dow, T. Huang, Appl. Catal. A: Gen. 218 (2001) 69–79.
[49] E. Ramírez-Cabrera, A. Atkinson, D. Chadwick, Catal. Today 36 (2002) 193–206.
[50] G. Zhou, L. Barrio, S. Agnoli, S.D. Senanayake, J. Evans, A. Kubacka, M. Estrella, J.C. Hanson, A. Martnez-Arias, M. Fernandez-Garca, J.A. Rodriguez, Angew. Chem. Int. Ed. 49 (2010) 9680–9684.
[51] S.D. Senanayake, J. Evans, S. Agnoli, L. Barrio, T.L. Chen, J. Hrbek, J.A. Rodriguez, Top. Catal. 54 (2011) 34–41.
[52] L. Barrio, A. Kubacka, G. Zhou, M. Estrella, A. Martınez-Arias, J.C. Hanson, M. Fernandez-Garcıa, J.A. Rodriguez, J. Phys. Chem. C 114 (2010) 12689–12697.
[53] B. Savova, S. Loridant, D. Filkova, J.M.M. Millet, Appl. Catal. A: Gen. 390 (2010) 148–157.
[54] E. Heracleous, A.A. Lemonidou, J. Catal. 237 (2006) 162–174.
[55] W. Xu, R. Si, S.D. Senanayake, J. Llorca, H. Idriss, D. Stacchiola, J.C. Hanson, J.A. Rodriguez, J. Catal. 291 (2012) 117–126.
[56] W. Xu, Z. Liu, A.C. Johnston-Peck, S.D. Senanayake, G. Zhou, D. Stacchiola, E.A. Stach, J.A. Rodriguez, ACS Catal. 3 (2013) 975–984.
[57] M. Mogensen, N.M. Sammes, G.A. Tompsett, Solid State Ion. 129 (2000) 63–94.
[58] H.C. Yao, Y.F. Yao, J. Catal. 86 (1984) 254–265.
[59] J.Z. Shyu, K. Otto, J. Catal. 115 (1989) 16–23.
[60] R. Wojcieszak, A. Jasik, S. Monteverdi, M. Ziolek, M.M. Bettahar, J. Mol. Catal. A: Chem. 256 (2006) 225–233.
[61] H.S. Roh, K.W. Jun, W.S. Dong, S.E. Park, Y.I. Joe, J. Mol. Catal. A: Chem. 181 (2002) 137–142.
[62] R.O. da Fonseca, A.A.A. da Silva, M.R.M. Signorellia, R.C. Rabelo-Neto, F.B. Noronha, R.C.C. Simões, L.V. Mattos, J. Braz. Chem. Soc. 25 (2014) 2356–2363.
[63] S.M. de Lima, A.M. da Silva, L.O.O. da Costa, J.M. Assaf, G. Jacobs, B.H. Davis, L.V. Mattos, F.B. Noronha, Appl. Catal. A: Gen. 377 (2010) 181–190.
[64] T.S. Moraes, R.C. Rabelo Neto, M.C. Ribeiro, L.V. Mattos, M. Kourtelesis, X.E. Verykios, F.B. Noronha, Top. Catal. 58 (2015) 281–294.
[65] A.N. Fatsikostas, X.E. Verykios, J. Catal. 225 (2004) 439–452.
[66] A.E. Galetti, M.F. Gomez, L.A. Arrua, M.C. Abello, Appl. Catal. A: Gen. 348 (2008) 94–102.
[67] M.C. Sanchez-Sanchez, R.M. Navarro, J.L.G. Fierro, Int. J. Hydrogen Energy 32 (2007) 1462–1471.
[68] E. Ramírez-Cabrera, A. Atkinson, D. Chadwick, Appl. Catal. B: Environ. 36 (2002) 193–206.
[69] Z. Hu, H. Nakamura, K. Kunimori, H. Asano, T. Uchijima, J. Catal. 112 (1988) 478–488.
[70] Z. Hu, H. Nakamura, K. Kunimori, Y. Yokoyama, H. Asano, M. Soma, T. Uchijima, J. Catal. 119 (1989) 33–46.
[71] J.R. Rostrup-Nielsen, J. Catal. 85 (1984) 31.
[72] G.L. Haller, D.E. Resasco, Adv. Catal. 36 (1989) 173–235.
[73] O. Khamman, R. Yimnirun, S. Ananta, Mater. Lett. 61 (2007) 639–643.